



FAKULTÄT FÜR **INFORMATIK**

Susceptibility Weighted Imaging with multiple echoes

DIPLOMARBEIT

zur Erlangung des akademischen Grades

Diplom-Ingenieur/in

im Rahmen des Studiums

Medizinische Informatik

eingereicht von

Christian Denk

Matrikelnummer 0726751

an der

Fakultät für Informatik der Technischen Universität Wien

Betreuung:

Ao.Univ.Prof. DI Dr.rer.nat. Dr.techn. Dr.scient.med. Frank Rattay

Mitwirkung: Dr. Alexander Rauscher; UBC MRI Research Centre

Wien, 04.02.2011

(Unterschrift Verfasser)

(Unterschrift Betreuer)

Christian Denk, Maurer Lange Gasse 101/11 1230 Wien

Hiermit erkläre ich, dass ich diese Arbeit selbständig verfasst habe, dass ich die verwendeten Quellen und Hilfsmittel vollständig angegeben habe und dass ich die Stellen der Arbeit einschliesslich Tabellen, Karten und Abbildungen, die anderen Werken oder dem Internet im Wortlaut oder dem Sinn nach entnommen sind, auf jeden Fall unter Angabe der Quelle als Entlehnung kenntlich gemacht habe.

Wien am 3.Februar 2011

Kurzfassung

Eines der erfolgreichsten Werkzeuge zur modernen Bildgebung ist die Magnetresonanztomographie (MRT). Mit der MRT sehen wir dem Gehirn beim Denken, dem Herz beim Schlagen, den Tumoren beim Wachsen zu. Ein wesentlicher Grund für den Erfolg der MRT ist die Tatsache, dass man neue Methoden entwickeln kann, ohne die Hardware des Scanners verändern zu müssen. Man kann also allein durch geschicktes Manipulieren der Atomkerne mit Magnetfeldern neue Wege der Bildgebung beschreiten.

Ein neuer Weg ist die suszeptibilitätsgewichtete Bildgebung (SWI) welches einen verstärkten Kontrast anhand Suszeptibilitätsunterschiede zwischen Substanzen produziert. Die Suszeptibilität ist die magnetische Antwort einer Substanz (z.B. Eisen) die innerhalb eines magnetischen Feldes plaziert wird. SWI verwendet im Unterschied zu konventionelle MRT Methoden zusätzlich die gewonnenen MRT Phasenbilder. Phasen geben wichtige Aufschlüsse über den Gewebestruktur und chemische Zusammensetzung. Durch das limitierte Intervall $[-\pi, \pi]$ der Phase entstehen Artefakte (Phasensprünge). Diese werden durch angepasste Nachaufbereitung beseitigt.

Die vorliegende Arbeit beschreibt die Erweiterung dieser SWI Standardsequenz mit der Aufnahme mehrfacher Echos bei gleichbleibender Akquisitionszeit (ME-SWI). Um diese beiden Sequenzen zu vergleichen wird das Signal zu Rauschen und das Kontrast zu Rausch Verhältnis in verschiedenen Gehirnsubstanzen gemessen. Durch die Messung mehrerer Echos gewinnt man 46% mehr Signal und erreicht 34 bis 80% mehr Kontrast. Mit dieser Sequenz kann gleichzeitig die MRT Phase sowie der Signalverlauf gemessen werden. Um Phasensprünge besser zu eliminieren wurde die Nachaufbereitung adaptiert und bei längeren Echozeiten grössere homodyne Filterung verwendet. Die Signalstärke oder Geweberelaxationszeit R_2^* konnte aus den Magnitudenbildern mit Korrektur auf Hintergrundfeldinhomogenitäten berechnet werden. Weiters wurde die Veränderungen des Signalverlaufs auf unterschiedliche Voxelgrößen oder räumliche Filterung untersucht. Grössere Voxel ergaben einen niedrigeren Signalverlauf und räumliche Filterung bis zu einem Volumen kleiner 16 mm^3 ergaben einen erhöhten Signalverlauf. Die Phase und der Signalverlauf wurden in einem Scan-Rescan Experiment auf ihre Variabilität untersucht. Es wurde gezeigt, dass die Phase signifikant bessere Reproduzierbarkeit gegenüber dem Signalverlauf aufweist. Das Ergebnis dieser MRT Sequenz sind schärfere Bilder, auf denen Venen mit Durchmessern von 0.1 mm sichtbar sind, und Karten des Eisengehaltes im Gehirn von Phase und Signalverlauf innerhalb nur eines Scans.

Abstract

One of the most successful imaging tools is magnetic resonance imaging (MRI). MRI makes movies of the beating heart, it observes mental processes in the brain or it visualizes the growth of tumours. An important reason for the success of MRI is that new methods can be developed without changing the hardware. Clever manipulation of the atomic nuclei with magnetic fields opens various windows into structure and function of biological tissue.

One new window is "Susceptibility Weighted Imaging" (SWI) which produces an enhanced contrast based on susceptibility differences between substances. Susceptibility is defined as the magnetic response of substances such as iron placed in an magnetic field. SWI additionally uses the MRI signal's phase in contrast to most other MRI techniques. Phase offers important information about the underlying tissue structure and chemical composition. Due to the phase's limited domain $[-\pi, \pi]$ artifacts or phase wraps arise. SWI uses a special post processing routine to get enhanced contrast and also uses the phase as an input.

In this master thesis the standard SWI sequence is extended to acquire multiple echoes (ME-SWI). To evaluate the newly developed sequence against the state of the art sequence the signal to noise and contrast to noise are calculated in different brain regions. Using multiple echoes 50% more signal and 34 to 80% more contrast can be achieved. With the ME-SWI method the MRI phase and signal decay is extracted simultaneously. The post processing to eliminate phase wraps is adapted using a greater homodyne filter kernel with increasing echo time. The signal decay or tissue relaxation time R_2^* is calculated from the magnitude images including a correction for background field inhomogeneities. Signal decay variation due to voxel geometry and spatial smoothing are investigated too. Larger voxel decrease the signal decay, while the decay with spatial smoothing up to a region volume of 16 mm^3 increases.

A scan-rescan experiment was performed to investigate the variability of the phase and signal decay. The coefficient of variation was calculated for all acquired data types (phase, magnitude, SWI, and R_2^*) to determine reproducibility. Phase showed a significant better reproducibility than the signal decay. The result of this sequence are sharper images, where venous vessels up to 0.1 mm are visualized and maps in form of the signal decay and MRI phase of brain iron content can be computed within one scan.

Contents

1. Introduction	3
I. Theory of NMR and MRI	5
2. Nuclear Magnetic Resonance	6
2.1. Atomic Nuclei	6
2.2. Relaxation Phenomena	9
2.3. Free Induction Decay FID	11
3. Magnetic Resonance Imaging	13
3.1. Slice Selection	14
3.2. Frequency Encoding	15
3.3. Phase Encoding	16
3.4. k -space	16
3.5. Field of View - FoV	18
4. Imaging Methods	20
4.1. Introduction	20
4.2. Spin-Echo Imaging (SE)	20
4.3. Gradient-Echo Imaging (GRE)	22
4.3.1. 3D Gradient Echo Imaging	23
II. Magnetic Susceptibility, Phase and R_2^*	25
5. Principles of susceptibility contrast	26
5.1. Magnetic Susceptibility	26
5.2. Magnetic Properties of Blood	28
5.3. The BOLD effect	28
5.3.1. Single Cylindric Vessel	28

6. Susceptibility Weighted Imaging	30
6.1. Introduction	30
6.2. SWI data acquisition parameters	30
6.3. Using phase information	31
6.3.1. Homodyne Filtering	31
6.3.2. Phase unwrapping	32
6.4. Phase mask and final SWI data	32
6.5. Minimal intensity projections	33
7. SWI with multiple echoes	34
7.1. Introduction	34
7.2. Data acquisition	35
7.3. Data processing analysis	36
7.4. Calculation of the Relaxation Time R_2^*	38
7.5. SNR & CNR comparison	39
7.6. Results	39
8. Reproducibility of phase and R_2^* using the multi echo SWI sequence	44
8.1. Introduction	44
8.2. Data acquisition	46
8.3. Data Processing	46
8.4. Regions of interest	47
8.5. Reproducibility	48
8.6. Spatial resolution and spatial smoothing	48
8.7. Results	49
9. Discussion	55
9.1. SWI with multiple echoes	55
9.2. Reproducibility of phase and R_2^*	58
Bibliography	64

1

Introduction

Magnetic resonance imaging (MRI) is the most powerful medical imaging technique these days. This imaging technique broadens its spectrum with permanent increase of applications and image processing tools.

This thesis focuses on susceptibility weighted imaging (SWI) which offers a new type of contrast in MRI compared to the typical T1 or T2 contrast. This modality not only uses magnitude image information, but also takes the phase data into account. Phase exploits and evaluates the magnetic properties of blood, iron and other tissue types and is very sensitive to small field-inhomogeneities, that are produced by magnetic susceptibility differences in structures. To produce an enhanced magnitude contrast phase and magnitude images are combined and reflect a contrast very sensitive to venous blood, hemorrhage and structures with high iron content. As this imaging method also relies on the BOLD (blood-oxygen-level-depend) effect, SWI was referred to BOLD venography in the beginning [1] [2]. SWI applications range from a variety of neurovascular and neurodegenerative diseases [3] trauma [4] [5], stroke [6] [7], cerebrovascular disease [8], venous anomalies [9], tumors [10] [11], Parkinson's disease [12] [13], multiple sclerosis [14] [15], Huntington's disease [16], Alzheimer disease [17], identifying breast calcifications [18], as well as examination of physiological processes [19] [20] [21].

The aim of the present work was to design a SWI sequence aiming to gain susceptibility contrast without increasing acquisition time. Therefore the standard SWI single echo gradient echo sequence was extended acquiring multiple echoes. Besides the gain in contrast and signal, the signal decay also could be extracted from the magnitude data. Using this post processing step the signal decay relaxation time R_2^* can be calculated. As phase's limited interval $[-\pi, \pi]$, the phase information has to be unwrapped. An adaption of the phase unwrapping routine to this sequence has been investigated too. Furthermore the reproducibility of this sequence extracted metrics phase, R_2^* , magnitude and SWI were evaluated with a scan rescan experiment. As R_2^* is used to assess brain-iron content the effects and change of R_2^* due to spatial smoothing or change in voxelsize have been investigated.

The first two introductory chapters explain the theory of NMR and MRI. The basic MRI methods are explained in chapter 4. Chapter 5 discusses the basic principles of susceptibility contrast and the properties of blood. The data acquisition parameters and post processing steps of SWI are introduced in chapter 6. The development of the sequence, it's parameters, the calculation of the relaxation time R_2^* are addressed in chapter 7. A comparison of the signal-to-noise ratio (SNR) and contrast-to-noise ratio (CNR) between the standard single echo SWI sequence and the multi echo SWI sequence are illustrated in the same chapter. Chapter 8 investigates the reproducibility of the multi echo SWI sequence metrics. This chapter furthermore exploits the effects of smoothing magnitudes images and the acquisition with different voxel-dimensions in aspect to the change of R_2^* and its reproducibility.

Part I.
Theory of NMR and MRI

2

Nuclear Magnetic Resonance

Introduction

The principle of nuclear magnetic resonance (NMR) was discovered independently by Bloch and Purcell in 1946. NMR uses the fact that every nucleus with an odd number of protons placed in a strong magnetic field can be excited to a higher energy level by an electromagnetic pulse. The excited spins then return back to the energy equilibrium and the absorbed energy is released. This retransmitted energy is measured in NMR. It provides information about the physical properties of the elements in the excited object. NMR is therefore used to obtain physical and chemical properties of the examined object. This chapter will explain the NMR basis. The next chapter will expound the important step from NMR to magnetic resonance imaging (MRI) to spatially encode the resonance signal so the exact spatial position of the signal can be decoded.

2.1. Atomic Nuclei

Each nucleus with a odd number of protons or neutrons (mass number A) has a nuclear angular spin momentum, called spin \mathbf{I} . That momentum acts like a small magnetic dipole. Table 2.1 presents typical nuclei and their

Atomic Number	Mass Number	I	$\frac{A}{Z}$ Nucleus
even	even	0	$^{12}_6\text{C}$, $^{16}_8\text{O}$
odd	odd	$\frac{1}{2}, \frac{3}{2}, \frac{5}{2}, \dots$	^1_1H , $^{15}_7\text{N}$, $^{19}_9\text{F}$, $^{31}_{15}\text{P}$
even	odd	$\frac{1}{2}, \frac{3}{2}, \frac{5}{2}, \dots$	$^{13}_6\text{C}$, $^{17}_8\text{O}$
odd	even	1, 2, 3, ...	^2_1H , $^{14}_7\text{N}$

Table 2.1.: Properties of some nuclei.

properties. As a result of the rotating charge, these nuclei have a magnetic moment μ ,

$$\mu = \gamma \hbar \mathbf{I}, \quad (2.1)$$

where γ is the gyromagnetic ratio and $\hbar = 6.6 \cdot 10^{-34}[\text{Jsec}]$ the Planck's constant for the specific nucleus. Without any external magnetic field the orientation of the spins and magnetic moments is random, which leads to zero net magnetization M_z (Fig. 2.1A). With an external static magnetic field \mathbf{B}_0 applied in one direction (throughout this report referred as the z-direction) the nuclei will align parallel (n_+) and anti-parallel (n_-) with the magnetic field \mathbf{B}_0 (Fig. 2.1B).

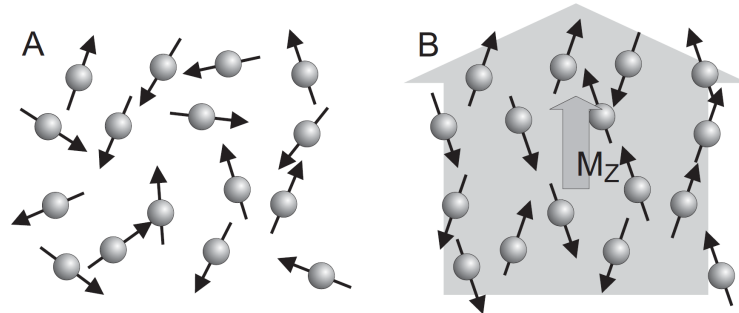


Figure 2.1.: A: Without external magnetic field \mathbf{B}_0 there is no net magnetization due to Brownian motion. B: Spins inside a magnetic field align parallel or anti-parallel to \mathbf{B}_0 [22].

The protons with magnetic vectors parallel to the magnetic field ($m_I = 1/2$) will have a slightly lower energy than the anti-parallel ($m_I = -1/2$) state, where the energy difference ΔE (Fig. 2.2A) is

$$\Delta E = \hbar \gamma B_0. \quad (2.2)$$

This is the energy needed to 'lift' or excite protons from their lower energy

level to their higher one. The exact ratio between the number of protons in parallel (n_+) and anti-parallel (n_-) state is given by the *Boltzmann* distribution

$$\frac{n_-}{n_+} = \exp\left(-\frac{\gamma\hbar\mathbf{B}_0}{k_B T}\right), \quad (2.3)$$

where $k_B = 1.3807 \cdot 10^{-23}$ J/K is the Boltzmann constant and T is the temperature. Since $n_+ > n_-$ (Eq. 2.3) it is clear that there is a non-zero total net magnetization vector \mathbf{M}_0 . The magnitude of \mathbf{M}_0 is the sum of the magnetizations of all the nuclei. The orientation of \mathbf{M}_0 is the same as the direction of the main magnetic field \mathbf{B}_0 (Fig. 2.2B).

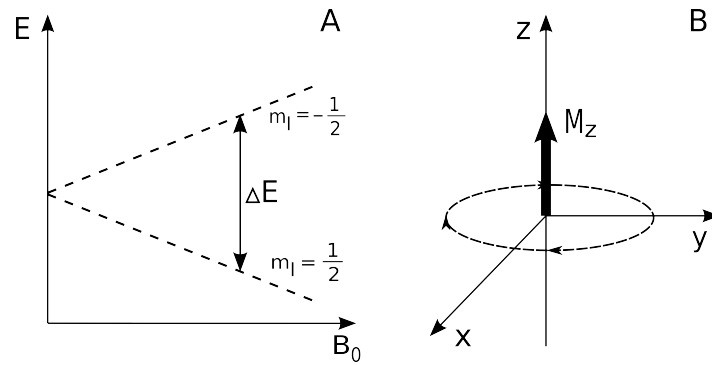


Figure 2.2.: A: The energy difference ΔE dependency to the magnetic field \mathbf{B}_0 . B: Net magnetization M_z produced by the differences $n_+ > n_-$ in direction of \mathbf{B}_0 .

The strength of the magnetization M_z (Eq. 2.2, 2.3) can be increased by lowering the temperature (this is not suitable for medical purposes) or by increasing the strength of the main magnetic field \mathbf{B}_0 . The spins can switch from the lower energy state to the higher energy state by an absorption of a photon. The energy of the photon must precisely match the energy difference ΔE between the two states. Since the energy of a photon is related to its frequency, thus only a photon with the exact frequency (called Larmor or resonance frequency) ω_L will cause the transition of the proton to the higher energy state. The resonance frequency ω_L of a proton is proportional to the strength of the external magnetic \mathbf{B}_0

$$\omega_L = \gamma \cdot \mathbf{B}_0 [\text{rad} \cdot \text{s}^{-1}]. \quad (2.4)$$

The frequency of precessing 1H atom in a 3 Tesla magnetic field is approximately $127.72 [\text{rad} \cdot \text{s}^{-1}]$.

2.2. Relaxation Phenomena

Applying a radio-frequency (RF) field B_1 which is perpendicular to the static magnetic field \mathbf{B}_0 and which rotates with a frequency ω about the z -axis

$$\mathbf{B}_1 = \begin{pmatrix} B_1 \cos \omega t \\ B_1 \sin \omega t \\ 0 \end{pmatrix}, \quad (2.5)$$

excites the spins. If ω is equal to the resonance or lamor frequency ω_L the energy amount reaches a maximum. Applying the RF field will lead to an angular excitation of the spins from the z -direction into the xy plane. Length and power of the RF field defines the amount or degree of excitation. A 90° degree pulse excites the spins parallel to the z -direction fully into the xy plane. The net magnetization M_z directly after the pulse is zero, but the magnetization in the xy plane reaches a maximum (transversal magnetization). After the RF field is applied, all excited spins will relax and return from the xy plane back to the z -direction. The magnetization returns in an exponential fashion with a time constant T_1 in order of 100-1000 *ms* back to the equilibrium and has specific values for different tissue types (Table. 2.2) [23].

Tissue	T_1 [ms]	T_2 [ms]
gray matter	950	100
white matter	600	80
muscle	900	50
fat	250	60
blood	1200	100-200
cerebrospinal fluid	4500	2200

Table 2.2.: Spin-lattice relaxation times T_1 and spin-spin relaxation times T_2 of several tissues at a field strength of 1.5 T. The T_2 is always shorter than T_1 (adopted from [23]).

The z -component $M_z(t)$ after the excitation is

$$M_z(t) = M_0(1 - e^{-t/T_1}), \quad (2.6)$$

where M_0 is the magnetization vector in the equilibrium state and T_1 is the *longitudinal* or *spin-lattice relaxation* time in milliseconds.

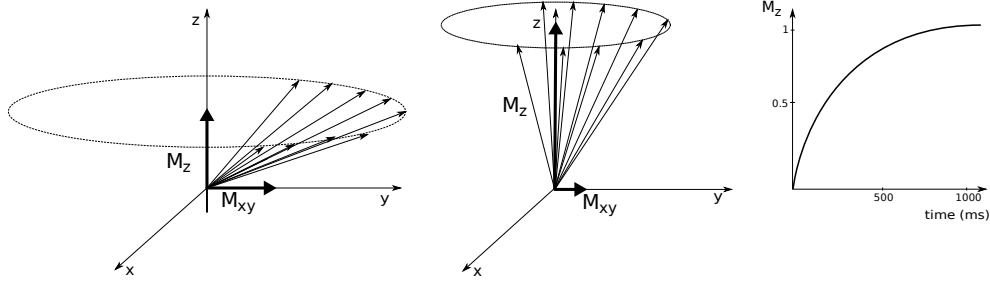


Figure 2.3.: (left) The spin-lattice relaxation is the reversion-process of the magnetization M_{xy} from the xy - plane towards M_z . The dephasing of the spins in the xy plane is observed at the same time M_z increases. This increase has an exponential decay with the time constant T_1 (right).

The dipole-dipole interaction between neighboring spins is the second type of relaxation, the so called *transverse* or *spin - spin relaxation*. Spins flipped into the xy -plane they start to precess with ω_L . In the beginning all spins precess phase-coherent, but with increasing time the spin-spin interaction and therefore different local magnetic fields destroy the phase-coherence of the single magnetic momentum. Some spins precess faster than the rotating frame with a frequency higher than ω_L and some precess at a lower frequency.

This leads to the exponential decay of the transversal magnetization M_{xy} with the transverse relaxation time T_2 (Fig. 2.4) (Table. 2.2)

$$M_{xy}(t) = M_{xy}(t_0)e^{-t/T_2} \quad . \quad (2.7)$$

Spin-lattice relaxation and spin-spin relaxation occur independently. T_1 is explained by the energy exchange with the lattice. T_2 is signal loss due to randomization of spin orientations. Both relaxation times T_1 and T_2 produce the mainly used image contrast mechanism in anatomical MRI.

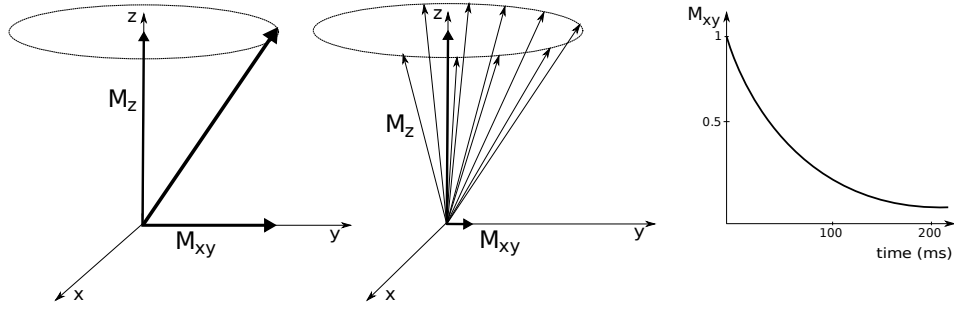


Figure 2.4.: (left) The destruction of the phase-coherence, due to different local magnetic fields decreases the magnetization M_{xy} in the xy -plane. Different spin environments (e.g. different tissues types: white and gray matter) will lead to differences in relaxation rates T_2 and provide contrast (right).

2.3. Free Induction Decay FID

The free induction decay (FID) can be explained in a simple one pulse experiment. Using a 90° RF pulse from $t = -tp$ and length tp in y direction, the net magnetization will reach a maximum at $t = 0$ in x direction (Fig. 2.5 (left)). The Magnetization in the three dimension are:

$$\begin{aligned}
 M_x(t) &= M_0 e^{-t/T_2} \cos \omega_L t \\
 M_y(t) &= M_0 e^{-t/T_2} \sin \omega_L t \\
 M_z(t) &= M_0 (1 - e^{-t/T_1}).
 \end{aligned} \tag{2.8}$$

The magnetization M_z and M_y will precess with the Larmor frequency ω_L around the static magnetic field \mathbf{B}_0 immediately after turning the pulse off. This leads to induction in the receiver coil. The induction will decrease exponentially with the already presented relaxation time T_2 . Fieldinhomogeneities of \mathbf{B}_0 lead to spatially variant field strengths and therefore to different Larmor frequencies. This yields also to further reduction of phase-coherence of the spins and to an additional magnetization loss of the transversal magnetization (Fig. 2.5). This additional signal loss mechanism is described by the relaxation time T_2^* :

$$\frac{1}{T_2^*} = \frac{1}{T_2} + \gamma \Delta B_0 = \frac{1}{T_2} + \frac{1}{T_2'} \quad , \tag{2.9}$$

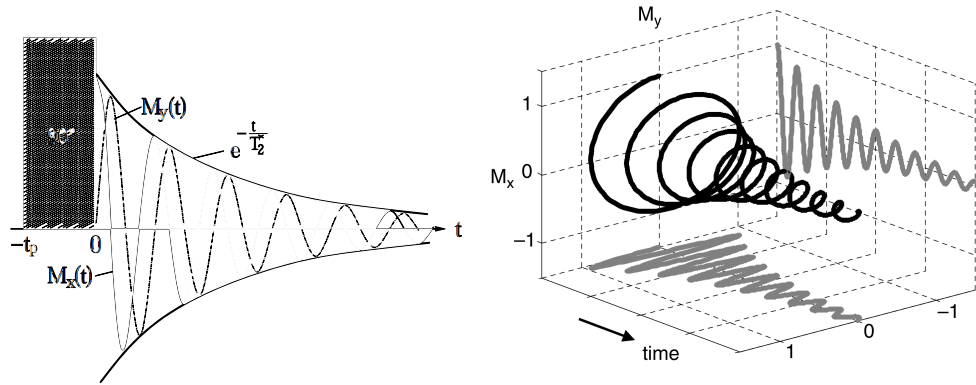


Figure 2.5.: (left) The exponential signal decay of the magnetization M_x (real part) and M_y (imaginary part) after a 90° RF pulse. The transverse magnetization precesses at the Larmor frequency and decays with a characteristic time constant T_2^* as time progresses. (right) A 3D visualization of the complex FID signal described by the two projections on M_x and M_y planes, corresponding to the real and imaginary components (adapted from [24]).

where ΔB_0 is the local field inhomogeneity of \mathbf{B}_0 and T_2' the time constant determined by spin dephasing in mesoscopic (i.e. with spatial frequencies corresponding to the size of a voxel) and macroscopic (i.e. with spatial frequencies corresponding larger than the voxel size) field inhomogeneities.

The trend of the induction signal intensity is called free induction decay or free induction signal (Fig. 2.5). The magnetization M_x and M_y are the real and imaginary part of the FID. The FID contains the whole nuclear spin information. This time domain information is converted to frequency domain applying the Fourier transform.

3

Magnetic Resonance Imaging

Introduction

MRI is probably the most important application of NMR. The important step from NMR to MRI is to spatially encode the resonance signal so the exact position of the signal can be decoded and images can be acquired. Magnetic field gradients are used to encode the position of the signal. A field gradient is an additional magnetic field, in the same direction as \mathbf{B}_0 , whose amplitude varies linearly with position along a chosen axis. The idea is that the field gradients imposed on the main magnetic field \mathbf{B}_0 will locally change the resonance frequency ω_L . To encode spatially in three dimension the field gradients have to be changed in strength and timing along the acquisition. The main magnetic field \mathbf{B}_0 is along the z direction, while magnetic field gradient are applied along any axis x, y, z :

$$G_x = \frac{dB_0}{dx}; G_y = \frac{dB_0}{dy}; G_z = \frac{dB_0}{dz} \quad (3.1)$$

3.1. Slice Selection

In order to select an xy plane with the slice thickness Δz a magnetic field gradient and an RF pulse are applied orthogonal (z direction) to this plane. The RF pulse with a sinc shape has a rectangular frequency-profile with a center frequency $\omega(z_0)$

$$\omega(z_0) = \gamma \cdot (B_0 + G_z \cdot z_0) \quad (3.2)$$

and a bandwidth of

$$\Delta\omega = \gamma \cdot G_z \cdot \Delta z. \quad (3.3)$$

Spins in the area from $z_0 - \frac{\Delta z}{2} \leq z \leq z_0 + \frac{\Delta z}{2}$ will be excited. The slice thickness varies with the bandwidth $\Delta\omega$ and/or the strength of the magnetic field gradient G_z (Fig. 3.1).

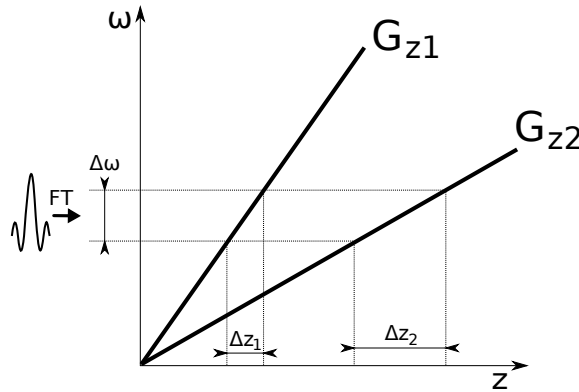


Figure 3.1.: The influence of the slice thickness Δz using different slice selection gradients G_z . The stronger gradient G_{z1} results in the thinner slice Δz_1 and vice versa.

3.2. Frequency Encoding

RF pulse and slice gradient selection excites a certain region, but there is no spatial encoding within the slice or slab yet. There are two ways to encode the signal spatially, the frequency encoding and the phase encoding. Spatial encoding along the x -axis is called frequency encoding (or encoding in the direction of the readout gradient). A magnetic field gradient G_x is applied along the x -axis after the RF pulse excitation and slice selection gradient G_z . The position on the x -axis corresponds now to the precession frequency and vice versa (Fig. 3.2).

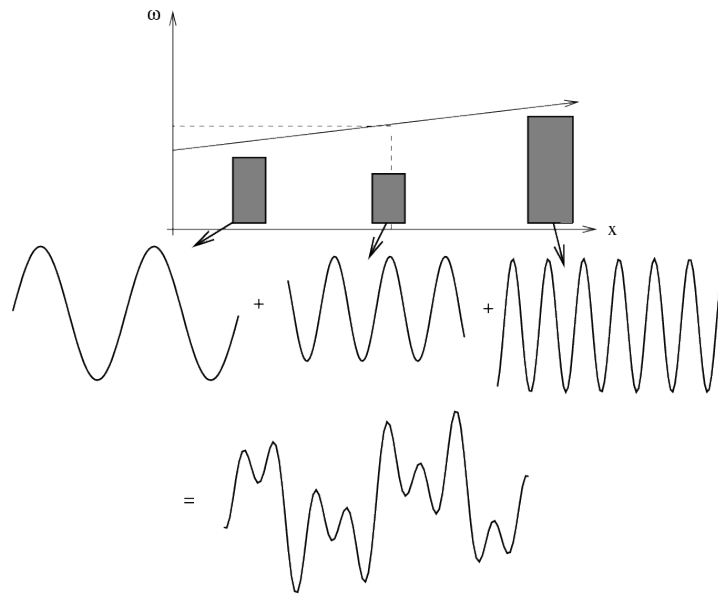


Figure 3.2.: Illustrates the effects of a frequency encoding gradient G_x . The three gray rectangles represent homogeneous samples with different location (x -direction) and different amounts of protons (represented by the dimensions of the rectangles). The frequency depends on the x -axis location and the amplitude is proportional to the amount of protons. The resulting signal of the three probes is displayed at the bottom [25].

The received signal in the receiver coils is a sum of harmonic functions with different frequencies and amplitudes. The amplitude is proportional with the proton density of a given voxel and the frequency describes the position on the x -axis. Since the frequency encoding experiment encodes position into frequency, the Fourier transformation of the signal is actually a one dimensional projection of the object along the gradient direction.

3.3. Phase Encoding

To encode the signal with phase encoding the spins phase is used as a function of position. A magnetic field gradient G_y is applied along the y -axis for a short time. This affects the precessing frequency. Spins at distinct spatial positions start precessing at slightly different frequencies. After the gradient is turned off the spins begin to precess again at the original frequency. But now these spins all have different phases. These phases now represent the spatial position along the y -axis (Fig. 3.3).

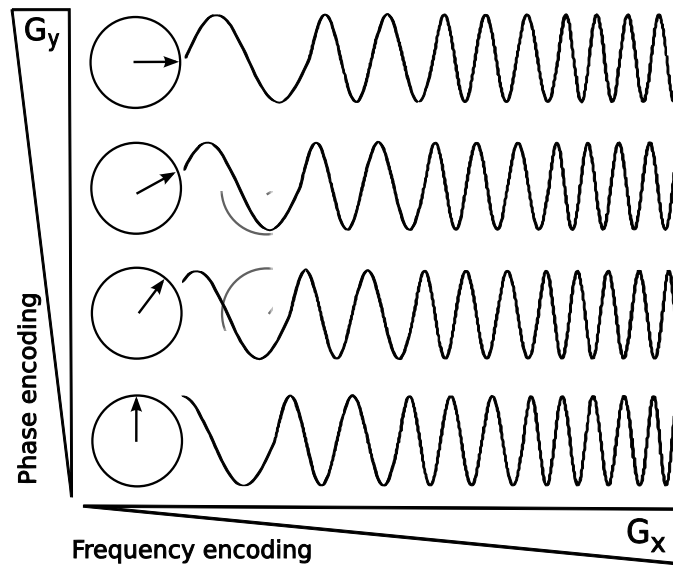


Figure 3.3.: Illustrates spatial signal encoding in two dimensions with frequency encoding along the x -axis applying the gradient G_x and phase encoding along the y -axis using the field gradient G_y . The black arrows represent the different phase values along the y direction and the sine waves present different frequencies along the x direction.

3.4. k -space

The measured MR signal depends on the gradient strength and timing, and result in the so called k -space or frequency space [26] [27]. One point \mathbf{k} in k -space is defined by the time characteristics of the gradients after the RF-pulse ($t = 0$)

$$\begin{aligned}
k_x &= \frac{\gamma}{2 \cdot \pi} \int_0^t G_x(t') dt', \\
k_y &= \frac{\gamma}{2 \cdot \pi} \int_0^t G_y(t') dt', \\
k_z &= \frac{\gamma}{2 \cdot \pi} \int_0^t G_z(t') dt'.
\end{aligned} \tag{3.4}$$

The k -space is represented by a matrix, where the MR-signal is placed in the corresponding location \mathbf{k} :

$$S(k_x, k_y, k_z) = \int \int \int p(x, y, z) e^{-i \cdot 2\pi \cdot (k_x \cdot x + k_y \cdot y + k_z \cdot z)} dx dy dz, \tag{3.5}$$

where p is the spin-density and a relaxation-time depending parameter. The way k -space is traversed and data acquired is called the k -trajectory. Trajectories are usually cartesian, spiral, radial or propeller sampling. One vector point k represents one point in k -space and describes a sine wave with the wavelength $\lambda = 2\pi/|\mathbf{k}|$ with perpendicular direction to the wave's front \mathbf{k} . The complex MR-signal is defined as \hat{p} and is a result of the waves superpositions. Mathematically this is described by the inverse Fourier transform of $S(k_x, k_y, k_z)$.

$$\hat{p}(k_x, k_y, k_z) = \int \int \int S(k_x, k_y, k_z) e^{i \cdot 2\pi \cdot (k_x \cdot x + k_y \cdot y + k_z \cdot z)} dk_x dk_y dk_z, \tag{3.6}$$

The Fourier Transform of k -space results in the desired MR-image. Data points in k -space are discrete and constrictive sampled. k -space trajectories describe the k -space sampling (Fig. 3.4 (right)). Sequence pulse diagrams are used to visualize the time elapsed of the applied gradients strength and RF-pulses (Fig. 3.4 (left)). Both tools together represent a convenient way to display complicated imaging acquisition. One example the spin-warp sequence [28] which is shown in Fig. 3.4: The positive slice selective gradient G_z slope excites a certain slice, the negative lobe of G_x brings the k -space trajectory to the k_x^{max} position. The G_y^i strength defines the corresponding k_y -position. The readout sampling of the echo and the applied positive G_x causes the trajectory travel from k_x^{min} (left) to k_x^{max} (right). This sequence is repeated with different G_y^i until the whole k -space is covered. Note that only discrete points in k -space and not continuous

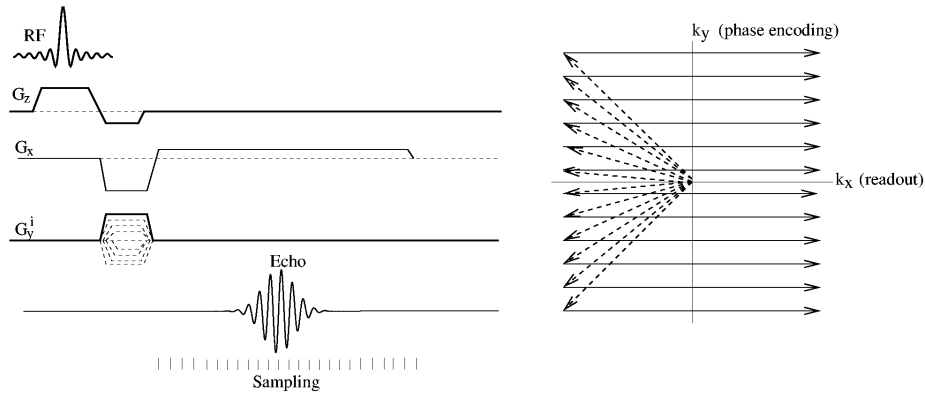


Figure 3.4.: Pulse diagram of the spin warp sequence and the corresponding trajectory in k -space. It is common to show only one excitation pulse, although as many RF-pulses as phase encoding gradients G_y have to be applied. The dashed arrows in the image of the trajectory correspond to the phase encoding steps G_y in the pulse diagram [25].

values are acquired.

3.5. Field of View - FoV

The two or three dimensional spatial encoding area of the image is defined as the field-of-view (FoV). The FoV is usually square or rectangular and contains the object of interest. It is defined by its size and position in the phase-encoding and the frequency-encoding direction. The discrete sampling of k -space and the use of the Fourier transform lead to consequences for the image and directly influence important image parameters:

- The image resolution of the image Δx , the distance between to calculated image points, where

$$\Delta x = \frac{2\pi}{FoV}. \quad (3.7)$$

The image resolution worsen the smaller the sampled area in k -space.

- The image dimensions (FoV)

$$FoV = \frac{2\pi}{\Delta k}, \quad (3.8)$$

the FoV gets smaller, the less data points in k -space are sampled.

Therefore the size of the FOV in the image space is related to the sampling distance Δk in k-space:

$$\Delta k = \frac{1}{FoV} \quad (3.9)$$

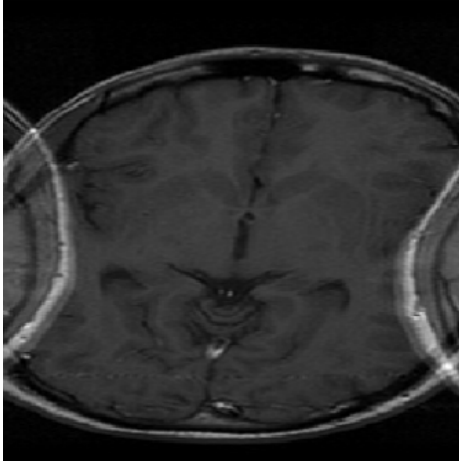


Figure 3.5.: Aliasing fold-over artifacts are produced by the acquisition of a too small FoV not covering the entire brain.

The position of the FoV can be adjusted by shifting the strength of the magnetic gradients. The resolution in the FoV is related to the range of the retrieved k -space values. Since the k -space image is the Fourier image of the slice values in k -space for higher k_y correspond to higher frequencies and therefore higher resolution. It is important to set the FoV to cover the whole imaged object, because parts of the imaged object that are not in the FoV are misinterpreted by aliasing (as being inside the FoV). This is due to the periodicity of the Fourier transformation. This effect is referred as the fold-over artifact (Fig. 3.5).

4

Imaging Methods

4.1. Introduction

MRI offers a variety of different contrasts underlying the usage of different pulses on gradient protocols. This chapter gives an overview of the most important basic imaging methods. Then, the standard imaging technique spin-echo imaging is presented, because of its broad use in MRI. The imaging technique gradient-echo (GRE) imaging as it was used for this work is explained in the chapter as well.

4.2. Spin-Echo Imaging (SE)

In spin echo imaging (SE) a 90° pulse is used to flip the magnetization vector to the transverse plane (Fig. 4.1). After the pulse, the magnetization vectors of all spins begin to dephase due to small inhomogeneities of the main magnetic field. After half the echo time $TE/2$, a 180° refocusing pulse is applied. Neglecting all the relaxation phenomena, this will cause the dephased magnetization vectors to flip around the y -axis in the transverse plane. The dephasing continues to happen in the same direction as before the 180° pulse. Consequently, after the second pulse the dephasing

effectively becomes rephasing. At TE , all the magnetization vectors are back in phase again emitting the maximal signal (Fig. 4.3). The advantage of this method is that the effects of static, time independent field inhomogeneities, resulting in T_2' , are compensated. Signal intensity at a certain TE in spin-echo imaging is always higher than in gradient-echo imaging, because T_2^* is always faster than T_2 (Fig. 4.2).

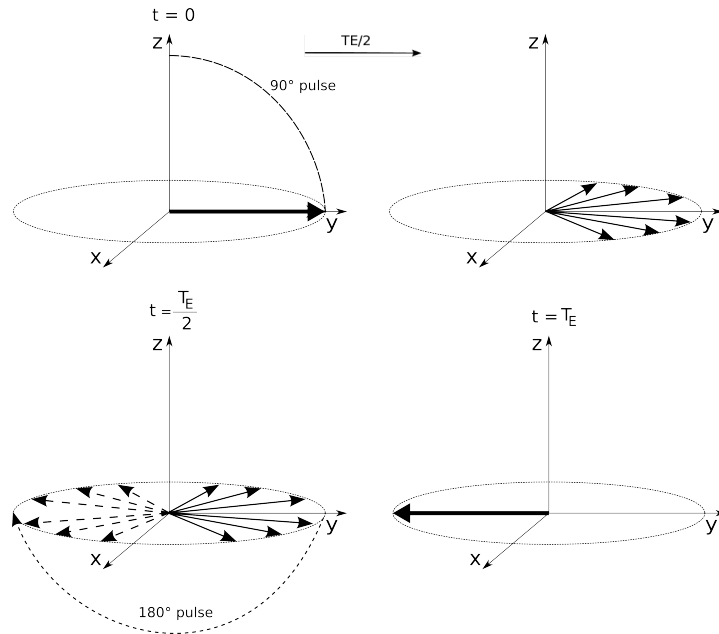


Figure 4.1.: A schematic presentation of the spin echo principle. After the 90° RF pulse the magnetic moments precess within the xy -plane. As time passes the moments will dephase due to field inhomogeneities (top row). A 180° pulse is used to set the slower moments in front of the faster. Hence the faster moments will form an echo at the same time as the slower moments (bottom row).

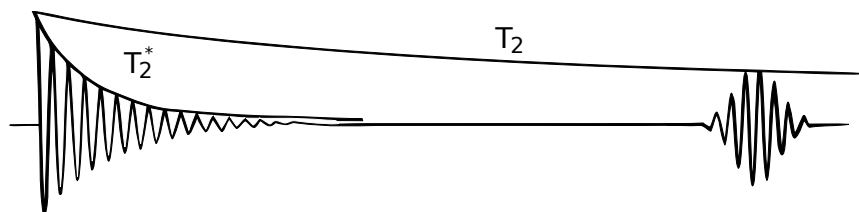


Figure 4.2.: The envelopes indicate the faster T_2^* and the slower T_2 signal decay and the spin echo at $t = TE$.

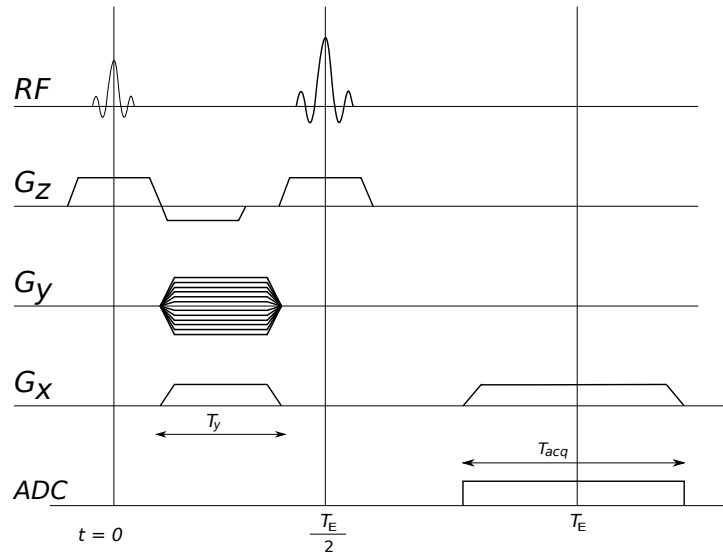


Figure 4.3.: Sequence pulse diagram with the usage of magnetic field gradients displaying the spin-echo sequence. The usage of the slice-selection G_z , the phase-encoding G_y and the read-out gradients G_x and the RF-pulses is shown.

4.3. Gradient-Echo Imaging (GRE)

The main difference between SE and GRE is the missing 180° pulse between excitation and data acquisition. Instead, gradient reversal on the frequency-encoded axis forms the echo (Fig. 4.4). After the 90° pulse excitation all magnetization is flipped into the xy-plane. First applying a frequency-encoding gradient with negative polarity will destroy the phase coherence of the precessing spins (*dephasing*). The same gradient is applied with opposite polarity which leads to *rephasing* of the spins to form a gradient echo. This pulse sequence is the simplest imaging sequence. Since no 180° refocusing pulse is needed to generate gradient echoes, very short repetition times (TR) can be achieved. As TR is a major determinant of the overall scan time of a GRE sequence and of most other sequences much faster imaging is possible compared with SE sequences. As a result, GRE sequences are less frequently troubled by motion artifacts and are thus preferred whenever a short scan time is desirable. Examples include vascular and cardiac imaging and acquisitions that require breath-holding. The missing 180° pulse in the SE leads to a rephasing of spins that were dephased

by mesoscopic field inhomogeneities (T_2'). As this pulse and the rephasing do not exist in gradient echo imaging this method is sensitive to static field inhomogeneities and the signal decays with T_2^* . The longer the selected TE the more accentuated T_2^* contrast is achieved. T_2^* weighted images are useful to detect calcifications or deposits of blood products in tissues with a very short T_2 such as connective tissues. GRE sequences are also used in conjunction with the administration of iron oxide-based contrast media. These effects are employed in susceptibility weighted imaging (SWI) and will be explained in detail in chapter 6.

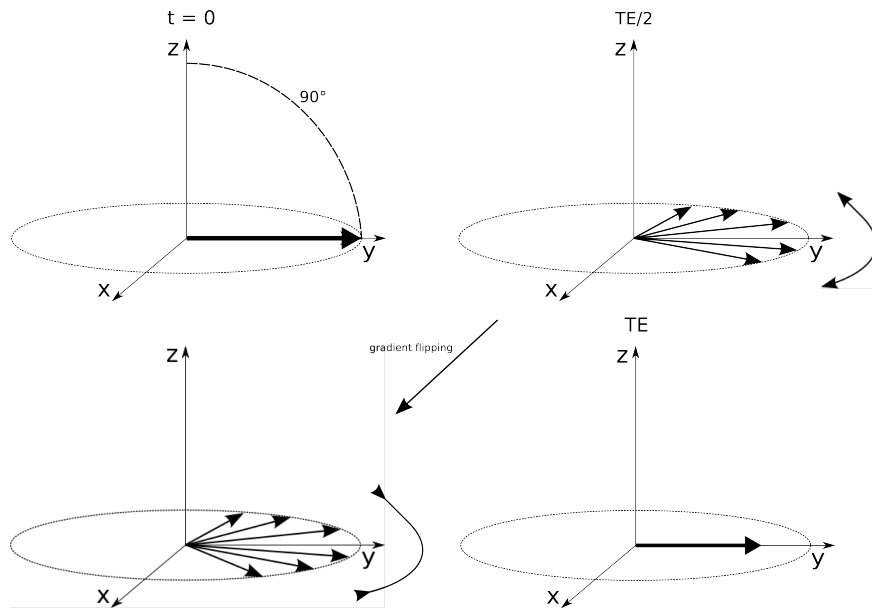


Figure 4.4.: A schematic illustration of the gradient echo sequence. After the 90° pulse the magnetic moments precess in the xy -plane and start dephasing due to an inhomogeneous field (top row). Flipping the sign of the dephasing or frequency encoding gradient spins start to rephase. Spins that precessed faster before, will precess slower and vice versus. This leads after $TE/2$ to the so called gradient echo (bottom row).

4.3.1. 3D Gradient Echo Imaging

The sequence used in this work is a high resolution 3D multi echo GRE SWI (see Chapter 7). This 3D imaging sequence excites a much thicker slab of slice, where the signal from each sub-slice is encoded by a second phase encoding gradient. Each RF-pulse excites the whole slab, but differ-

ent phase-encoding gradients encode the signal in z -direction. After this encoding step the rest of the sequence remains the same. As an interleaved acquisition is not possible with a second phase encoding, the repetition times (T_R), the time between two RF pulses, have to be short to get acceptable total acquisition time. This leads to small flip angles (FA typically 15° to 25°). Thin slices lead to decreasing intra-voxel T_2^* and short TE to higher MR-signal. Further partial volume effects are increased for very small objects, which is necessary for the application of SWI and the visualization of small venous vessels. Small flip angles lead to low specific absorption rates (SAR), which defines the amount of RF-pulse energy used in a sequence. The total acquisition time T_{acq} for a 3D gradient echo sequence is defined as

$$T_{acq} = (N_{phase_y} \cdot N_{phase_z} \cdot T_R) \cdot N_{avg}, \quad (4.1)$$

where N_{phase} is the number of phase encoding steps in y and z -direction and N_{avg} the number of averages.

Part II.

Magnetic Susceptibility, Phase and R_2^*

5

Principles of susceptibility contrast

5.1. Magnetic Susceptibility

Magnetic susceptibility is defined as the magnetic response of a substance when it is placed in an external magnetic field. The induced magnetization \mathbf{M} of an object inside a magnetic field is defined by

$$\mathbf{M} = \chi \mathbf{H}, \quad (5.1)$$

where χ is the magnetic susceptibility and \mathbf{H} is the magnetic field strength. The magnetic induction \mathbf{B} is related to \mathbf{H} by

$$\mathbf{B} = \mu_0(\mathbf{H} + \mathbf{M}) = \mu_0(1 + \chi)\mathbf{H} = \mu\mathbf{H}, \quad (5.2)$$

where μ_0 is the magnetic permeability of free space and $(1 + \chi)$ is the relative permeability of the material and represents the change of the magnetic field B inside the material. Diamagnetic substances show a $\chi < 0$, substances with $\chi > 0$ are called paramagnetic, when $|\chi| \ll 1$. When $|\chi| \gg 1$ the substances are referred to as ferromagnetic for positive χ and anti-ferromagnetic for negative χ .

Placing a sample with two materials of different magnetic susceptibilities inside a static magnetic field leads to change in the magnetic field inside

and outside the sample. An example for a spherical sample is shown in Fig. 5.1.

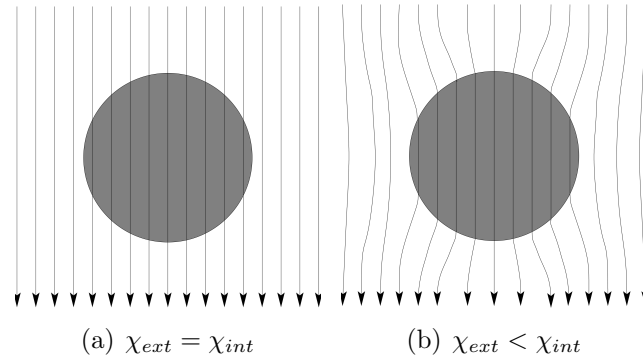


Figure 5.1.: A substance with χ_{int} is placed into a medium with χ_{ext} which leads to a distortion of an external magnetic field (adapted from [25]).

Heterogeneous susceptibility distribution leads to local field inhomogeneities, resonance frequency shifts and therefore phase changes and signal loss. These effects of inhomogeneities of the magnetic field can be categorized into three groups depending on the measured voxelsize [29].

Magnetic fieldinhomogeneities	Effects & application
microscopic \ll voxelsize	dynamic MRI with usage of a contrast agent (shortening of T_1)
mesoscopic \leq voxelsize	visualization of venous vessels, iron as well as calcifications due to signal loss inside a voxel (T_2^* shortening)
macroscopic \geq voxelsize	local effects at air/tissue boundaries or global effects due to static magnetic fieldinhomogeneities

Table 5.1.: The effects on the MR-signal due to magnetic fieldinhomogeneities relating to the acquisition voxel dimensions.

5.2. Magnetic Properties of Blood

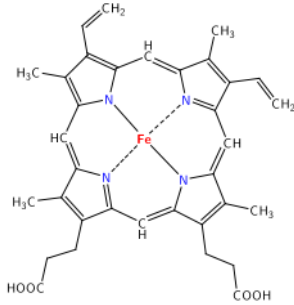


Figure 5.2.: The heme.

The transport of oxygen and carbondioxide is the a main purpose of blood. Blood consists of erythrocytes, thrombocytes, leukocytes and plasma. The functional group in erythrocytes, on which O_2 and CO_2 bind is the protein haemoglobin (Hb). Hb consists of four polypeptides with a heme attached to each of them (Fig. 5.2) and one atom of iron at the center of each heme. Each heme can bind one molecule of oxygen. If oxygen is bound to the heme the molecule is called oxyhemoglobin(HbO_2), otherwise it is referred to as deoxyhemoglobin (Hb). The magnetic properties of HbO_2 found to be diamagnetic whereas Hb is paramagnetic [30]. The magnetic susceptibility of erythrocytes with oxyhaemoglobin is $\chi_{HbO_2} = -9.19$ ppm and erythrocytes with deoxyhemoglobin have a susceptibility of $\chi_{Hb} = -6.7$ ppm [31]. Only pure haemoglobin is paramagnetic $\chi = +0.2$ ppm. T_2 relaxation-times are different of oxygenated and desoxygenated blood. T_2 is 100 ms for venous and 200 ms for arterial blood at 1.5T [23]. T_1 otherwise remains the same.

5.3. The BOLD effect

The *Blood Oxygenation Level Dependent* (BOLD) - effect [32] [33] is based on the susceptibility differences $\Delta\chi$ between oxygenated and deoxygenated blood. The MR-signal is dependent on the venous blood oxygenation level. $\Delta\chi$ between venous blood and surrounding tissue is

$$\Delta\chi = \chi_{do} \cdot Hct \cdot (1 - Y). \quad (5.3)$$

where Y is the oxygen saturation, Hct is the Hematocrit and $\chi_{do} = 2.35$ ppm the difference between fully oxygenated and completely deoxygenated blood [31]. The BOLD effect is the basis of venography with SWI and functional magnetic resonance imaging (fMRI).

5.3.1. Single Cylindric Vessel

To compute the magnetic field inside B_{int} and outside B_{ext} of a blood vessel, the vessel will be modeled as a cylinder of infinite length with a magnetic

susceptibility χ_{int} , embedded in a medium of susceptibility χ_{ext} [34]

$$\begin{aligned} \mathbf{B}_{int} &= \left[1 + \frac{\chi_{ext}}{3} + \frac{\chi_{int} - \chi_{ext}}{6} (3 \cos^2 \theta - 1) \right] \mathbf{B}_0 \\ \mathbf{B}_{ext} &= \left[1 + \frac{\chi_{ext}}{3} + \frac{\chi_{int} - \chi_{ext}}{2} \sin^2 \theta \frac{a^2}{r^2} \cos 2\phi \right] \mathbf{B}_0, \end{aligned} \quad (5.4)$$

where a is the radius of the vessel, θ is the angle between the vessel and the static magnetic field \mathbf{B}_0 . The angle ϕ describes the angle in the xy -plane (Fig. 5.3a). The field inside the vessel is independent of ϕ . The field is homogeneous with the same precession frequency. The intra- and extravascular field distribution as given in Eq. 5.4 are visualized in Fig. 5.3b, with $\theta = 30^\circ$ to the static magnetic field. At $\theta = 54.73^\circ$ the internal field is zero ($3 \cos^2 54.73^\circ - 1 = 0$) and therefore equal the field far away from the vessel. B_{ext} is inhomogeneous for all $\theta \neq 0^\circ$.

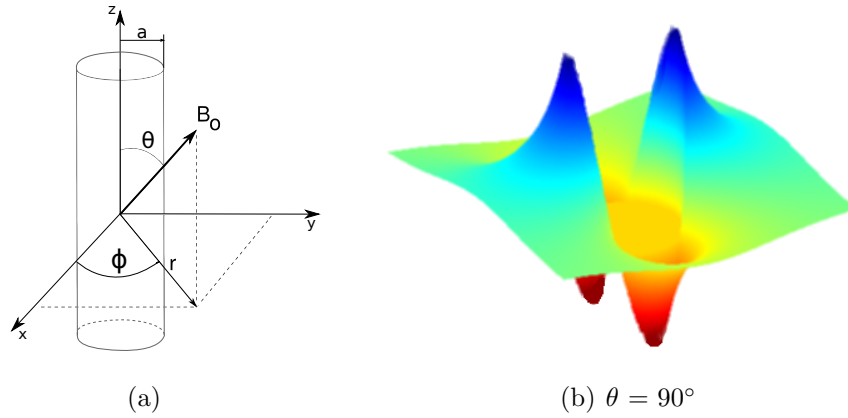


Figure 5.3.: (a) Model of a blood vessel in an external magnetic field with parameters.(b) Magnetic field distribution of a cylinder perpendicular to \mathbf{B}_0 (adapted from [25]).

These magnetic field changes can be detected in phase using sequences which are sensitive to small magnetic field changes, such as gradient-echo sequences (section 4.3). The intravascular, but especially extravascular field distortions seen in Fig. 5.3b, lead to a strong signal loss inside a voxel. These distortions allow the visualization of smallest vessels of a diameters around $100 \mu m$ even if the vessels cover a small portion of the voxelvolume.

6

Susceptibility Weighted Imaging

6.1. Introduction

MRI uses different contrast mechanism to distinguish between tissue types or chemical compositions. As shown in the previous chapter magnetic susceptibility of blood depends on the degree of oxygenation. This dependency can be used to create additional contrast to T_1 or T_2 . Not only blood but also susceptibility differences due to tissue iron content [35], calcification or hemosiderin can be utilized to generate contrast. This new contrast mechanism is called susceptibility weighted imaging (SWI). The image acquisition and the data post processing will be explained in this chapter.

6.2. SWI data acquisition parameters

SWI typically uses a 3D gradient echo sequence with flow compensation in all three gradient directions, hence moving spins in venous vessels and arteries are acquired. For the visualization of small venous vessels high resolution image have to be acquired to maximize the partial volume effects, where the occupied volume of the vein should be large within a voxel. To display small veins of diameter down to $100 \mu m$, typical acquisition matrices of 512 (readout) \times 512 (phase in y -direction) \times $50 - 80$ (phase in z -direction) voxels are necessary. Typical TE at 3T are 20-30 ms and a TR of 30-50 ms

to obtain good susceptibility contrast. Due to strong T_2^* weighting and long TE the sequence is sensitive to small local magnetic field changes. The flip angle which excites the longitudinal magnetization into the xy plane has a maximal SNR at the Ernst angle. Typical flip angles at 3T are around 15° to 25° .

6.3. Using phase information

The MR signal is a complex value having a magnitude and phase at all data points. Mainly magnitude signal values from GRE sequences are used for clinical purpose. What distinguishes SWI from conventional GRE imaging is that the phase of the signal is incorporated to obtain images with improved contrast. The phase contains valuable information [36] and has a higher SNR compared to the corresponding magnitude [37]. Both magnitude and phase of the susceptibility weighted data are sensitive to local variations in tissue magnetic susceptibility. These changes in the magnetic field are mapped into the phase's limited domain ($\pi \leq \phi < \pi$). The resulting ambiguities are usually referred to as phase wraps. The field inhomogeneities and therefore the number of phase wraps scale with field strength and with echo time. The elimination of phase wraps is either performed by the standard method homodyne filtering [38] or in image space using phase unwrapping method [39] [40] [41].

6.3.1. Homodyne Filtering

The complex MR image $I(x, y)$ is first convolved with a low pass filter kernel (L_p)

$$I_{LP}(x, y) = F_{LP} \bullet I(x, y) \quad (6.1)$$

to produce a filtered complex image. Dividing the original image I by the filtered image I_{LP} results in a high pass filtered image I_{HP} [38]. The reduced unwrapped phase images are obtained by computing the arctan of the division of the imaginary by the real part of the high pass filtered image I_{HP} :

$$\phi = \arctan \left(\frac{\text{Imag}[I_{HP}]}{\text{Real}[I_{HP}]} \right). \quad (6.2)$$

With increasing low pass filter kernel size, more lower frequencies are passing. This leads to better contrast in the resulting high pass filtered images

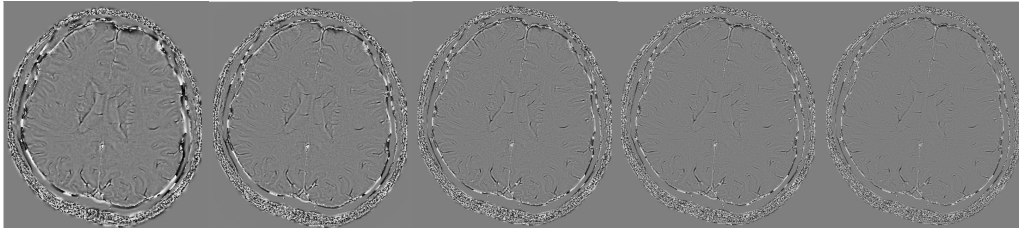


Figure 6.1.: Increasing homodyne filter kernel ranging from left to right from 0.2% to 0.6% of k -space data with an increment of 0.1% per image. With increasing kernel size, higher frequencies are blocked, which leads to reduced contrast of structures, but more phase wraps are eliminated especially along the borders of the brain.

of low spatial frequency structures, but also to more remaining phase wraps in low field inhomogeneities (Fig. 6.1).

For SWI at 1.5 T with a TE of 40 ms it was found that a window width of about 20 to 25 % of the respective k -space dimension results in sufficient phase wrap suppression and good susceptibility contrast [42].

6.3.2. Phase unwrapping

This phase correction is based on an image space region growing algorithm [39] [40] [41]. The phase wraps are eliminated by adding multiples of 2π to the corresponding pixels. Starting points are defined where the phase is locally smooth. The unwrapping of each pixel is based on a slope prediction obtained from its already unwrapped neighbors using as many neighbors as possible. The whole concept of this algorithm is to guide the region growing along the most reliable paths to deal with difficult areas as late as possible and to use as much neighbouring pixel as possible. Phase unwrapping preserves all spatial frequencies in contrast to homodyne filtering, where low spatial frequencies are removed.

6.4. Phase mask and final SWI data

The unwrapped or homodyne filtered phase images are used to create a phase mask which will be multiplied into the magnitude images to create the final SWI dataset where contrast is enhanced in defined structures. The phase mask is defined between 0 and 1, where positive phase values (white matter (WM), cerebral spinal fluid (CSF)) are set to 1 and negative values (veins, gray matter (GM) or tissue with high iron content) are scaled

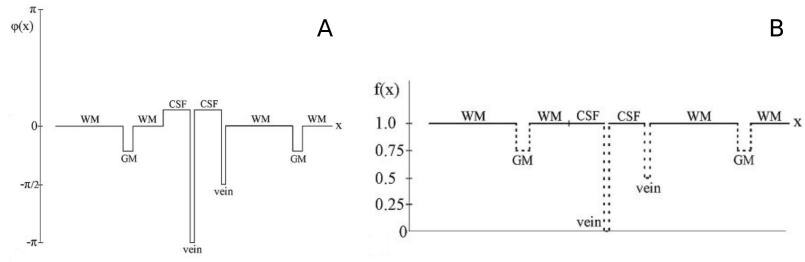


Figure 6.2.: A: typical phase values of different tissue types. B: Phase scaled from 0 to 1 to create the phase mask (adapted from [43]).

between 1 to 0. The phase mask can be applied multiple times with the magnitude image. A optimized contrast was found when multiplying the mask four times with the magnitude [2]. Veins with phase of $-\pi/2$ to $-\pi$ result in almost the same phase mask value after four multiplications.

6.5. Minimal intensity projections

To visualize and follow venous vessels minimal intensity projections (mIP) over a stack of slices are created. The minimum over slices ranging from z_1 to z_2 at every pixel (x, y) is taken (example illustrate in Fig. 7.8):

$$I_{mIP}(x, y) = \min(I_{SWI}(x, y, z))_{z \in [z_1, z_2]}. \quad (6.3)$$

7

SWI with multiple echoes

7.1. Introduction

Gradient echo techniques are widely used in MRI. Applications include among others, vascular imaging, 3D volume imaging and heavily T_2^* weighted imaging. Gradient echo imaging is fast and has low specific absorption rates due to small flip angles and the absence of refocusing pulses. The T_2^* relaxation time is very sensitive to changes in magnetic susceptibility. Iron as a source of susceptibility variations is of particular interest [44], since it is a potential marker for pathologies such as Parkinson disease [12] [13], Huntington disease [16], Alzheimer disease [17], or multiple sclerosis [14] [15]. The T_2^* decay is sensitive not only to tissue properties but also to background field inhomogeneities generated by air-tissue and bone-tissue interfaces or by imperfect shim. Therefore, the measured decay also depends on imaging parameters such as voxel size and slice orientation. The decay can be corrected for the unwanted influence from background inhomogeneities [45] [46]. Multi echo GRE imaging has been used to probe brain tissue for its iron content [47] [48] and even for its myelin content [48].

The susceptibility weighted phase can be used to assess brain iron content [49] and to visualize brain anatomy in high detail [36] [37]. Since both T_2^* and phase have the potential to assess brain iron content it seems a worthwhile goal to acquire both types of information in one scan. The

aim of this study was therefore to combine quantitative T_2^* measurements with the capabilities of SWI [50] [2]. SWI was thus acquired with multiple echoes. The phase correction by homodyne filtering was optimized for each individual echo by adapting the size of the filter window. Maps of $R_2^* = 1/T_2^*$ relaxation were computed from the magnitude of the data. The phase was used to compute field maps to correct the R_2^* maps from background inhomogeneities. SNR and contrast to noise ratio (CNR) were compared between single echo SWI and the proposed multi echo technique.

7.2. Data acquisition

Data from four healthy volunteers with no history of neurological or psychiatric diseases were acquired after obtaining informed written consent. This work used a multi echo gradient echo sequence [51] [47] [52] [53] where not only at one TE a gradient echo signal was acquired, but at different TE a

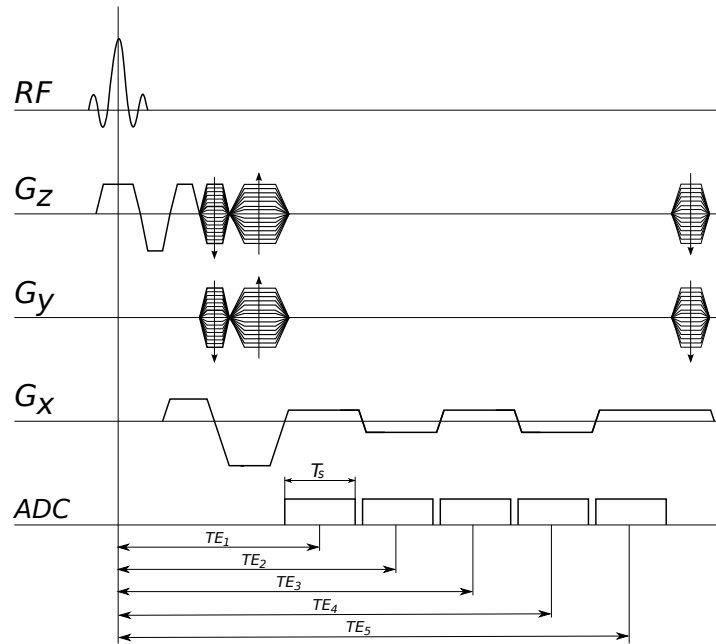


Figure 7.1.: Pulse diagram of a 3D Gradient echo sequence with multiple echoes. The usage of the slice-selection G_z , the phase-encoding G_y and the read-out gradients G_x , the RF-pulses and the ADC (analog digital converter, data acquisition), is shown. The read-out gradients alters its polarity according to the data sampling window with its sampling time T_s at each TE .

gradient echo was induced by the frequency encoding gradient. The pulse sequence is displayed in Figure 7.1. After the data is acquired at five different TE , RF spoiling is applied. Spoiling gradients represent gradient lobes on one or more axes that dephase any residual transverse magnetization before the next RF pulse.

Multi echo SWI data were acquired on a Philips Achieva 3T system equipped with an 8 channel head coil using a 3D gradient echo sequence. Five echoes with TE ranging from 13–41 ms and an interval of 7 ms were acquired with gradients of alternating polarity [53]. The first echo is fully flow compensated, whereas the third and fifth echo are flow compensated only in readout direction. Due to the sequence configuration there is no flow compensation on the second and fourth echo.

Further scan parameters were: TR = 45 ms, FA = 17 ° and a readout bandwidth (BW) of 157 Hz/pixel; FOV = 210 × 60 × 160 mm³ ; spatial resolution = 0.5 × 0.75 × 1.5 mm³ (voxel volume = 0.56 mm³) for the acquisition and 0.41 × 0.41 × 0.75 mm³ for the reconstruction with a matrix of 512 × 512 × 80 voxels. The average scan duration was 6.7 minutes. For comparison of SNR and CNR a single echo scan with the same spatial resolution (TE = 20 ms, TR = 45 ms, FA = 17°, readout BW = 110 Hz/pixel, acquisition time 6.6 minutes) was acquired. In one subject an additional scan with a spatial resolution of 0.4 × 0.6 × 1.5 mm³ (voxel volume = 0.36 mm³) was acquired and reconstructed to 0.32 × 0.32 × 0.75 mm³.

7.3. Data processing analysis

All image processing was performed using MATLAB (The MathWorks, Inc., Natick, MA) and FSL (FMRIB, Oxford, UK) on a personal computer with 8 Gb of memory running GNU/Linux. Magnitude and phase of the data were reconstructed on the MRI scanner using Sensitivity Encoding (SENSE) [54].

For SWI processing [50] [2] (Fig. 7.2) a symmetrically centered 2D Hanning low pass frequency filter was applied in a sliced by slice manner to the 2D k-space data. For TE = 20 ms a filterwidth (FW) of 0.25 of the k-space dimension was used. With increasing TE the spatial density of phase wraps increases. Thus FW adaption for different TE was explored. The FW of 0.25 at TE = 20 ms was used as a reference [42]. For longer TE the FW was increased so that the residual phase wraps were comparable to the situation at TE = 20 ms. The low pass filtered phase images were

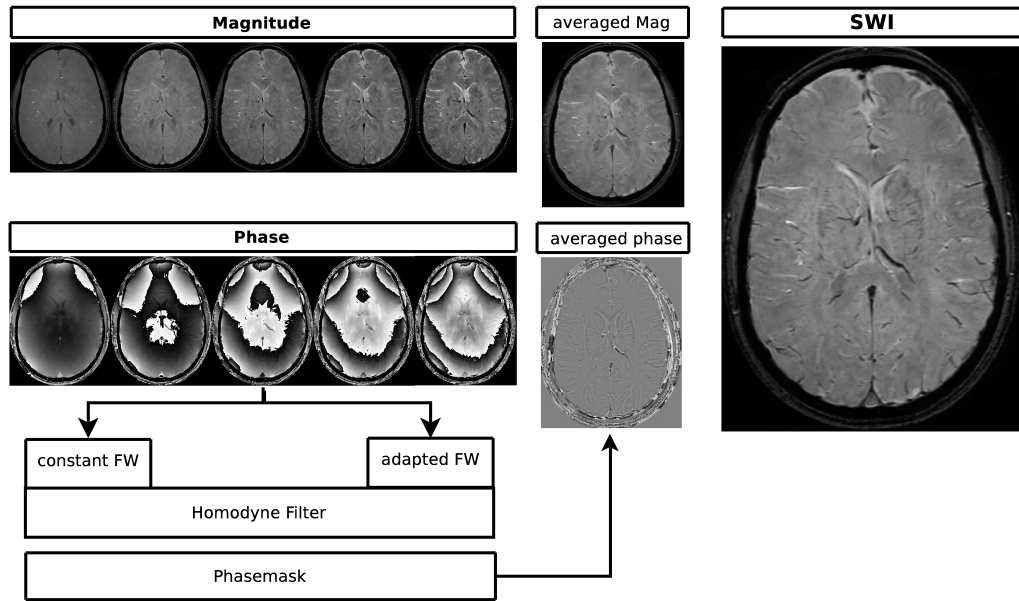


Figure 7.2.: Illustrates the SWI processing starting with the five acquired magnitude and phase images. A homodyne filter with constant filterwidth (FW) and echo time adapted FW were used to filter the phase images. The phasemask is multiplied with the power of four into the averaged magnitude which results in the SWI image with enhanced visibility of venous vessels.

subtracted from the original phase images using complex division to produce high pass filtered phase images. The assessment of the filter effect was based on visual inspection of the resulting phase images. The filtered phase images were converted into a negative phase mask. The fourth power of the mask was multiplied with the corresponding magnitude images to obtain the final SWI for each individual echo [50] [2]. Finally, the SWI of the five echoes were averaged.

7.4. Calculation of the Relaxation Time R_2^*

Maps of R_2^* relaxation rates were computed from the five magnitude images using a Levenberg- Marquardt least squares method for non-linear equations. The entire R_2^* post processing procedure is shown in Figure 7.3.

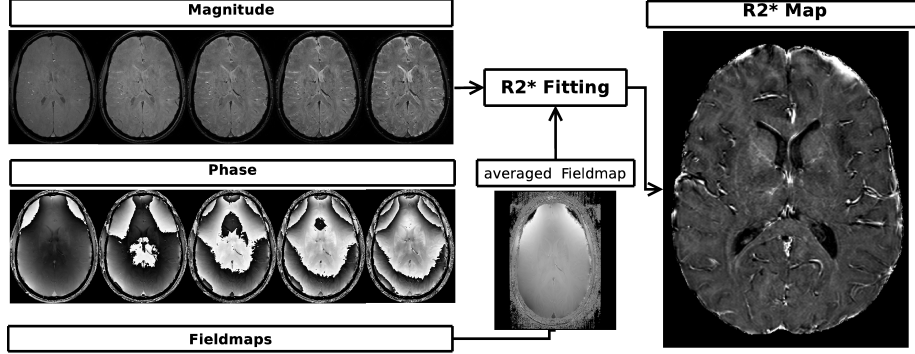


Figure 7.3.: Fieldmaps were calculated according to Eq. 7.1. R_2^* maps were computed from the five magnitudes with the sinc-term correction by [45] [46].

Figure 7.4 illustrates the signal decay for voxels of different tissue types. Magnitude data points and the calculated fitted curves are displayed. To correct for signal decay due to background field inhomogeneities the method proposed by Fernández-Seara and Wehrli [45] and extended by Dahnke and Schäffter [46] was used, which assumes a constant gradient in through plane direction. The field map required for this approach was calculated from the unwrapped phase $\Delta(TE_{i+1}, TE_i)$ (using the ΦUN tool [39] of the complex division from data of subsequent echo times TE_{i+1} and TE_i):

$$\Delta B_{i,i+1} = \frac{1}{\gamma (TE_{i+1} - TE_i)} \cdot \Delta \tilde{\varphi}, \quad (7.1)$$

where gamma is the gyromagnetic ratio of the proton. To improve SNR of the field map, the average of the four possible $\Delta B_{i,i+1}$ was computed. R_2^* was determined by fitting the following Equation.

$$S_{\Delta B_0}(TE) = S_0 \cdot e^{-TE \cdot R_2^*} \cdot \left| \frac{\sin(\gamma \cdot \Delta B_0 / 2 \cdot TE)}{(\gamma \cdot \Delta B_0 / 2 \cdot TE)} \right|, \quad (7.2)$$

where $S_{\Delta B_0}(TE)$ is the magnitude signal intensity at TE ; S_0 is the signal intensity at $TE = 0$ and ΔB_0 is the linear field variation. The sinc-term component in Eq. 7.2 is used for the correction of the influence from background field inhomogeneities.

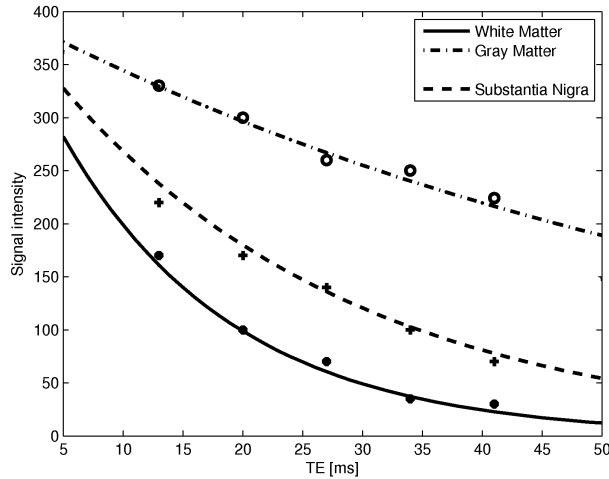


Figure 7.4.: Magnitude signal intensities for the five acquired echoes (datapoints) and the fitted R_2^* curves for a voxel in WM, GM and the substantia nigra (SN). R_2^* was for WM = 20 ms^{-1} , GM = 15 ms^{-1} and SN = 40 ms^{-1} .

7.5. SNR & CNR comparison

The single echo data were co-registered to the multi echo data using FSL by first registering the magnitude and then applying the registration parameters to the real and the imaginary part of the data. Phase images and SWI were then reconstructed from the registered complex data. SNR and CNR were determined for the single echo data and the combined magnitude images of the multi echo data. SNR was determined in six different regions in WM. SNR increase was calculated for each region separately and then averaged. CNR was defined as signal intensity differences between two neighboring tissue types, divided by the standard deviation of noise. CNR was evaluated between WM and the following structures: GM, putamen (Pu), corpus callosum (CC), optic radiation and veins. The standard deviation of a different region in the CC was used as a measure of noise.

7.6. Results

The effects of constant versus adaptive homodyne filtering are shown in Fig. 7.5 for phantom data and Fig. 7.6 for in-vivo results. With the standard filter width of 0.25 for all echo times phase wraps started to appear at a TE of 34 ms and degrade the final SW image.

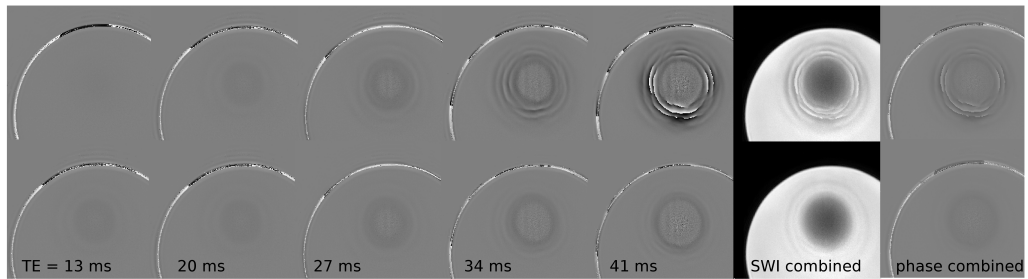


Figure 7.5.: Filtered phase images of the first to the fifth echo computed with a constant filter width of 0.25 (top row) and adapted filter widths ranging from $FW = 0.2$ at 13 ms to $FW = 0.4$ at 41 ms with increments of 0.05 (bottom row). Within the constant filter width phase wraps are present in the later echo times (34 and 41 ms) and in the combined phase and SWI, whereas the adapted filter successfully reduces phase wraps at all echo times. Note that the strong field inhomogeneities lead to signal loss in the magnitude due to intravoxel spin dephasing, which becomes apparent in the final SWI images.

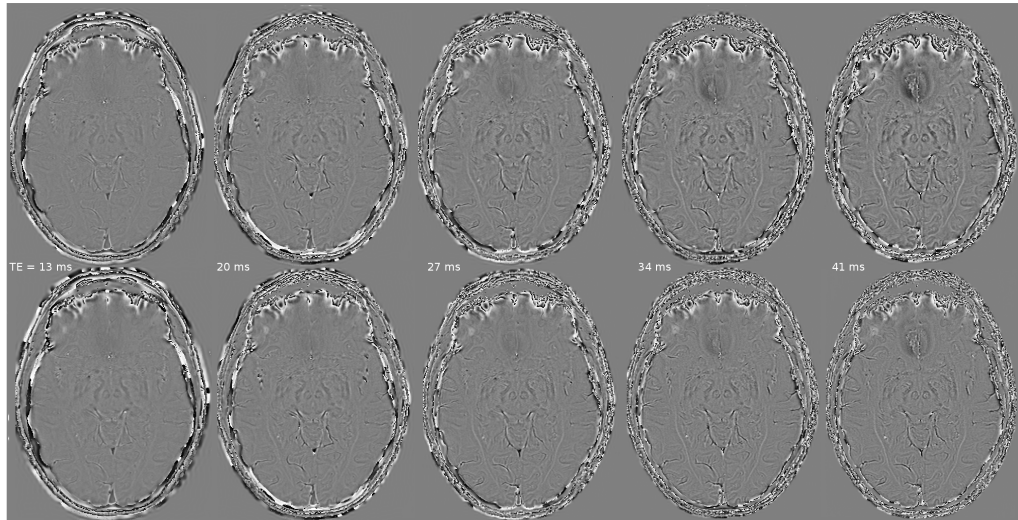


Figure 7.6.: Phase images of the first to the fifth echo produced with a constant width of the homodyne filter (top row) and filter widths adjusted to the echo times (bottom row). Adaptation of the filter width ($FW = 0.2$ at 13 ms to $FW = 0.4$ at 41 ms with increments of 0.05) results in a reduction of residual phase wraps.

Adapted filter widths ranging from 0.2 at $TE = 13$ ms to 0.4 at $TE = 41$ ms with increments of 0.05 for every additional 7 ms ($FW = 0.05/7 \cdot TE + 0.107$) resulted in good suppression of phase wraps and good phase contrast. With the adaptive filter the susceptibility contrast in the phase was similar for all

echo times (Fig. 7.6). Combined multi echo magnitude images had better SNR and CNR than their single echo counterpart (Fig. 7.7 and Table 7.1).

ROI	CNR [%]	SNR [%]	R_2^* [ms^{-1}]
white matter	-	46 ± 54	19.7 ± 1.1
gray matter	37 ± 49	-	15.2 ± 2.1
putamen	75 ± 137	-	27.1 ± 1
corpus callosum	66 ± 49	-	23.9 ± 1.0
optic radiation	80 ± 123	-	21.1 ± 1.0
veins	34 ± 50	-	47.3 ± 8

Table 7.1.: Increase in SNR and CNR and extracted R_2^* values.

Small veins were better visible and less blurred in the multi echo images than in the single echo images. SNR increased by about 50 % and CNR increased by 34 to 80 %, depending on the tissue type Table 7.1. R_2^* values extracted from the four volunteers are compared with R_2^* values by Péran et al. [55], Du et al. [52] and Krüger and Glover [56] (Table 7.2).

ROI	R_2^* [ms^{-1}]	R_2^* Literature values [ms^{-1}]		
		Perán [55]	Du [52]	Krüger [56]
white matter	19.7 ± 1.1	18.7 ± 1.7	23.0 ± 5.5	20.4 ± 1.2
gray matter	15.2 ± 2.1	14.2 ± 3.9	-	21.6 ± 1.7
putamen	27.1 ± 1	25.1 ± 2.2	29.0 ± 8.9	-
corpus callosum	23.9 ± 1.0	-	-	-
optic radiation	21.1 ± 1.0	-	-	-
veins	47.3 ± 8	-	-	-

Table 7.2.: Extracted R_2^* values compared to R_2^* values from literature

Minimum intensity projections over 7.5 mm of the magnitude, the phase, the venogram and the R_2^* of the high resolution scan are shown in Fig. 7.8. The R_2^* map (Fig. 7.8D) and the phase image (Fig. 7.8B) displayed the best contrast between GM and WM. The values for R_2^* ranged between 15ms^{-1} in GM and 47ms^{-1} in the optic radiation. Areas of large R_2^* (bright) coincided with venous vessels visible in the venograms.

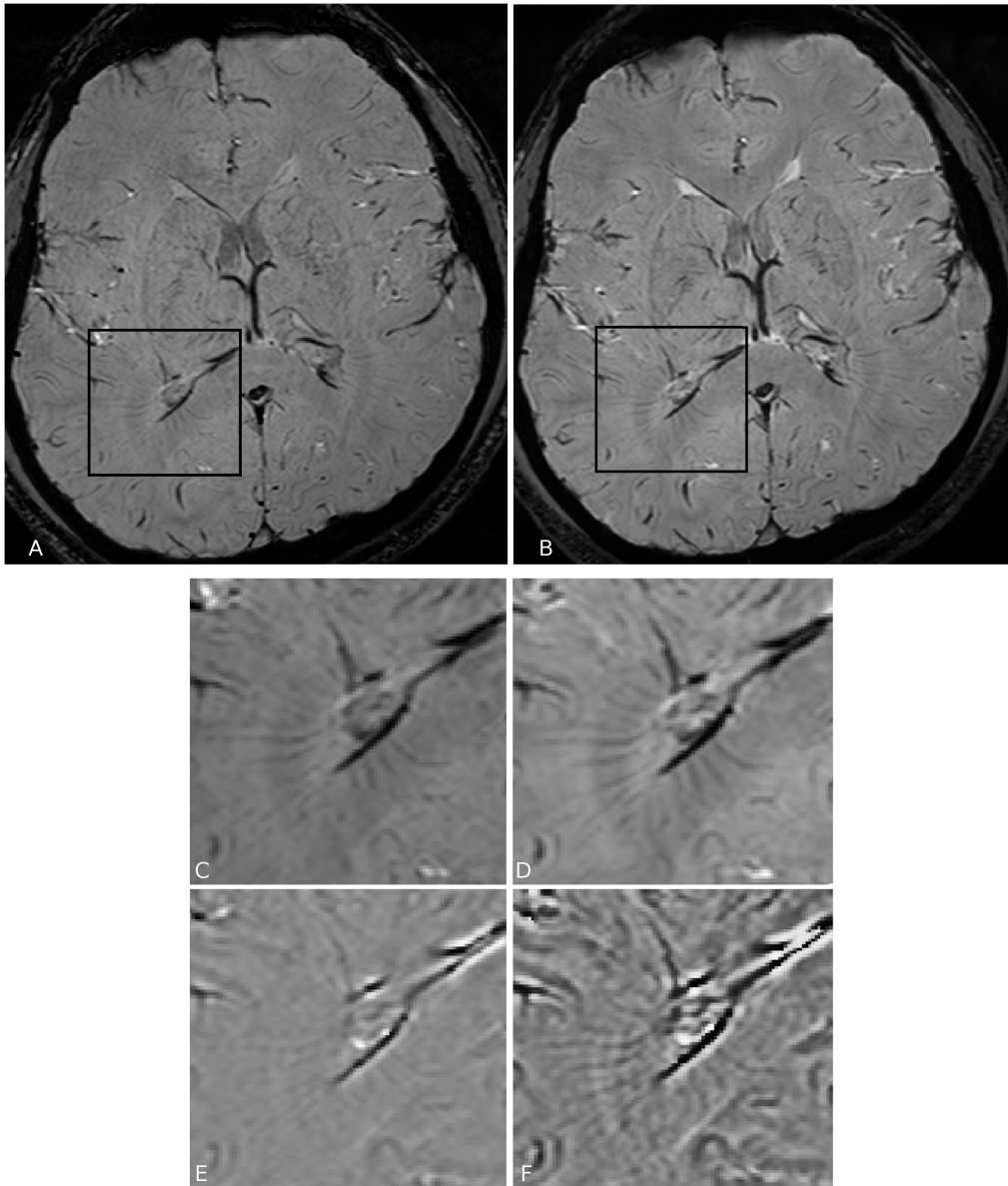


Figure 7.7.: One slice of the single echo SWI (A) and the combined five-echo SWI (B). The zoomed areas show magnitude and phase of the single echo data (magnitude in C, phase in E) and the combined multi echo data (magnitude in D, phase in F). Visibility of small veins, SNR and CNR are improved in the multi echo data (D,F) compared to the single echo images (C,E). Signal dropout in the frontal regions is slightly increased in the multi echo image. CSF in the SWI multi echo appears brighter, due to their short T_2^* .

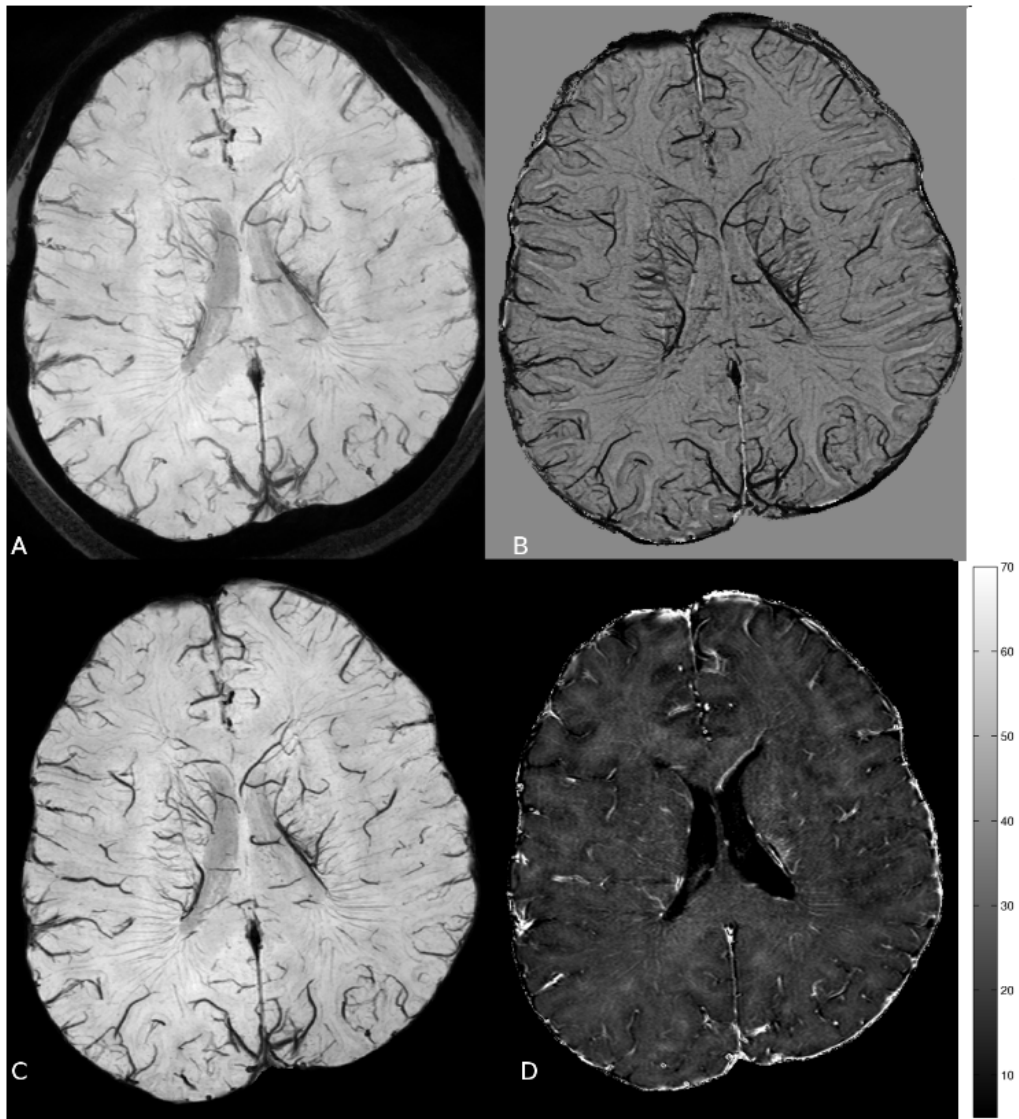


Figure 7.8.: Minimum intensity projections over 7.5 mm (10 slices) of the magnitude (A), the phase (B) and the SWI (C) of the combined 5 echoes of the high resolution scan (voxelsize $0.32 \times 0.32 \times 0.75 \text{ mm}^3$). The R_2^* map of the center slice of the stack is shown in D. Small subependymal veins are visible in all 4 images. Contrast between grey matter and white matter is best in the phase image and in the R_2^* map.

8

Reproducibility of phase and R_2^* using the multi echo SWI sequence

8.1. Introduction

Gradient-echo MRI is sensitive to changes in the magnetic susceptibility of tissue due to diamagnetic or paramagnetic substances. From the MRI point of view, the most important diamagnetic substance in the human body is calcium [57] [58] and the most important paramagnetic substances are heme and nonheme iron [44] [59]. Nonheme iron is of particular interest, because it is a strong modifier of magnetic susceptibility and it is associated with several neurological disorders, such as Parkinson's disease [12] [13] Alzheimer's disease [60] [17], Huntington's disease [16], and multiple sclerosis [14]. GRE techniques are attractive because they can be performed in three dimensions at acceptable acquisition times and they have a low SAR, which becomes important with the increasing number of scanners with field strengths of 7T and above. Gradient echo images provide phase images and, if acquired with multiple echo times, maps of R_2^* relaxation. The phase not

only provides images with good tissue contrast [36] and higher SNR compared to the corresponding magnitude [37], but also gives information on the magnetic susceptibility of tissues. One example, is the correlation with brain iron content [49] [61] [62]. Also the R_2^* maps generated from multi echo GRE data allow us to obtain information on tissue iron content, for example in Parkinson’s disease [63] [64] [47].

The high sensitivity of GRE imaging to changes in local field strength is also a drawback: background field inhomogeneities and their spatial relationship with the imaging geometry, in particular voxel aspect ratio and slice orientation, have an influence on R_2^* relaxation and phase. For some geometries analytic models exist from which it be can determine the magnetic susceptibility with high precision. Venous vessels, for instance, can be modeled as straight cylinders. If the spatial relationship between the cylinder, the imaging voxel and the main magnetic field is known, blood oxygenation for a particular vein can be calculated [65] [19]. In general, the tissue geometry is rather complex so that no analytical model exists. Moreover, background field inhomogeneities produced by air tissue and tissue bone interfaces or by imperfect shim have an additional effect on phase and signal decay of GRE scans. A simple and effective way to control the influence from background inhomogeneities is to use a high spatial resolution [66], which explains the success of high resolution techniques, such as SWI [66] [1] [2] and the success of GRE imaging at very high field strengths [20] [37]. The abundant SNR at ultra high fields allows for very small voxel sizes, which leave little room for the spatially slowly varying background field inhomogeneities. In the phase, these components can be removed by high pass filtering [38] [67].

The effect on the T_2^* decay can be compensated by measuring the background field inhomogeneities and including their influence in the fit of the signal decay [45] [46]. However, some of the background may still leak into the final result for two reasons: 1) The cut off frequency of the high pass phase filter is arbitrary and usually chosen to result in good phase contrast without any visual influence from the background. 2) The correction for additional R_2^* decay only accounts for constant through plane gradients, but not for more complex field inhomogeneities. Therefore head orientation and the imaging geometry may still have an influence on the phase and the magnitude of GRE MRI. This can make it difficult to compare results between different experiments if different voxel geometries or post processing strategies were used. Even within a study with uniform post processing, there may be variations which are not tissue specific but due to effects from

background inhomogeneities.

The purpose of this work was therefore twofold: First, the reproducibility of the metrics derived from multi echo GRE measurements will be investigated. In particular, I was interested in a comparison of phase and R_2^* , the two most important GRE metrics. Second, I investigated how variations of spatial resolution during data acquisition and spatial smoothing during post processing influence these metrics.

8.2. Data acquisition

Twelve healthy volunteers (mean age 34 years, range 20 - 53 years) with no history of neurological or psychiatric diseases were recruited. Informed written consent was obtained from each subject prior to the experiment. Multi echo SWI data were acquired twice (referred to Scan A and Scan B) on a Philips Achieva 3T system equipped with an 8 channel head coil using a 3D gradient echo sequence. The time period between scan A and B was one to four days. Five echoes with TE ranging from 13 - 41 ms and an echo interval of 7 ms were acquired with gradients of alternating polarity. The first echo is fully flow compensated, the third and fifth echo are flow compensated only in readout direction and the second and fourth echo are not flow compensated. Further scan parameters are: TR = 45 ms, FA = 17° and a readout BW of 157 Hz/pixel; FOV = $210 \times 60 \times 160$ mm³; spatial resolution = $0.5 \times 0.75 \times 1.5$ mm³ (voxel volume (VV) = 0.56 mm³) for the acquisition and $0.41 \times 0.41 \times 0.75$ mm³ (VV = 0.12 mm³) for the reconstruction with a matrix of $512 \times 512 \times 80$ voxels. The scan duration was 6.7 minutes. The AC-PC (anterior-posterior commissure) line was taken as the reference for both scans. In scan B, no special precautions were made to reproduce the head position and orientation from scan A.

8.3. Data Processing

All image processing was performed using MATLAB (The MathWorks, Inc., Natick, MA) and FSL (FMRIB, Oxford, UK [68]) on a personal computer running GNU/Linux. Magnitude and phase of the data were reconstructed on the MRI scanner using SENSE [54].

The scans were coregistered by registering the magnitude of the first echo and then applying the registration parameters to the real and the imaginary part of all echoes. Phase and magnitude images were then reconstructed

from the registered complex data. For SWI processing [1] [2] a symmetrically centered 2D Hanning low pass frequency filter [38] with adapted filter size (0.2 of k -space data at $TE = 13$ ms with increments of 0.05 for each later echo) was applied in a sliced by slice manner to the 2D k -space data [51]. The low pass filtered phase images were subtracted from the original phase images using complex division to produce high pass filtered phase images. The filtered phase images were converted into a negative phase mask [2]. The fourth power of the mask was multiplied with the corresponding magnitude images to obtain the final venogram for each individual echo. Finally, averages from the five echoes were calculated for the magnitude, phase and the venogram.

Maps of R_2^* relaxation rates were computed from the five magnitude images using a Levenberg- Marquardt least squares method for non-linear equations. A correction for signal decay due to background field inhomogeneities was performed using the method proposed by Fernández-Seara and Wehrli [45] and extended by Dahnke and Schäffter [46].

8.4. Regions of interest

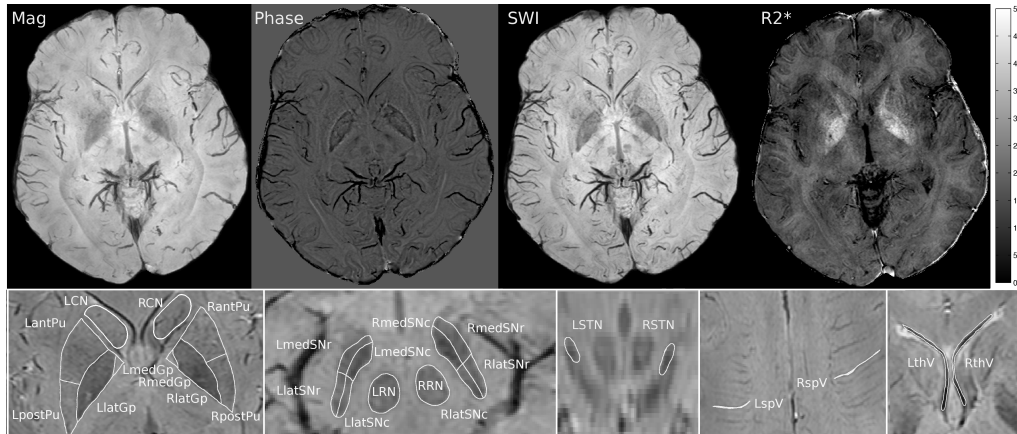


Figure 8.1.: Upper row from left to right: Minimum intensity projection (mIP) over 4.5 mm (6 slices) of the combined magnitude, phase, SWI and the calculated R_2^* map. Bottom row: Representative ROIs in the basal ganglia, structures in the deep brain and venous structures (highlighted in white).

Twentyeight regions of interest (ROIs), as shown in Figure 8.1, were drawn separately in each volunteer using FSL. In the deep brain, ROIs were placed

in the substantia nigra (SN), the red nucleus (RN) and in the subthalamic nucleus (STN). The SN pars compacta (SNc) and pars reticulata (SNr) were subdivided into a medial (med) and lateral (lat) component. In the midbrain, ROIs were drawn in the globus pallidus (Gp), the putamen (Pu), the caudate nucleus (CN) and CC. The Gp was subdivided into the medial and lateral part. Pu and the CC were divided into a posterior (pos) and an anterior (ant) part [47]. To assess reproducibility of the data in the presence of venous vascular structures, the thalamostriate vein, with a diameter larger than the voxel size, and a subependymal vein, with a diameter smaller than the voxel size, were identified. All listed structures were drawn onto both hemispheres, labeled as left = L and right = R in all tables and figures. The mean and standard deviation (SD) were calculated for each ROI in the five echoes in phase, magnitude, SWI and in the combined phase, magnitude, venogram as well as in the calculated R_2^* maps. A total number of 19 metrics in 28 ROIs in twelve subjects were investigated.

8.5. Reproducibility

To examine reproducibility of the different metrics, the coefficient of variation (COV) between scans A and B was calculated as the mean of the standard deviations σ of the two scans A and B divided by the mean (indicated by a bar) of the mean of the ROIs

$$COV = \frac{\overline{(\sigma_{ROIA}, \sigma_{ROIB})}}{\overline{(ROIA, ROIB)}} \quad (8.1)$$

All COV values presented within are averages over all subjects.

8.6. Spatial resolution and spatial smoothing

To simulate the effects of data acquisition with lower spatial resolution, 3D Gaussian smoothing of the complex data (labeled GC) was performed with kernel widths of $3 \times 3 \times 2$, $5 \times 5 \times 3$ and $7 \times 7 \times 5$ voxels. To investigate the effects of spatial smoothing Gaussian (G) and median (M) filters with kernel sizes of $3 \times 3 \times 2$, a $5 \times 5 \times 3$ and $7 \times 7 \times 5$ voxels were used. COV and R_2^* values were calculated for all ROIs and all filtering techniques.

8.7. Results

Figure 8.2 displays the mean \pm SD COV of the 19 metrics (R_2^* , phase, magnitude and venograms of the 5 echoes and the combined magnitude, phase and venogram) of the left lateral part of the SNc. The COV of the magnitude, phase and venogram increases with echo time.

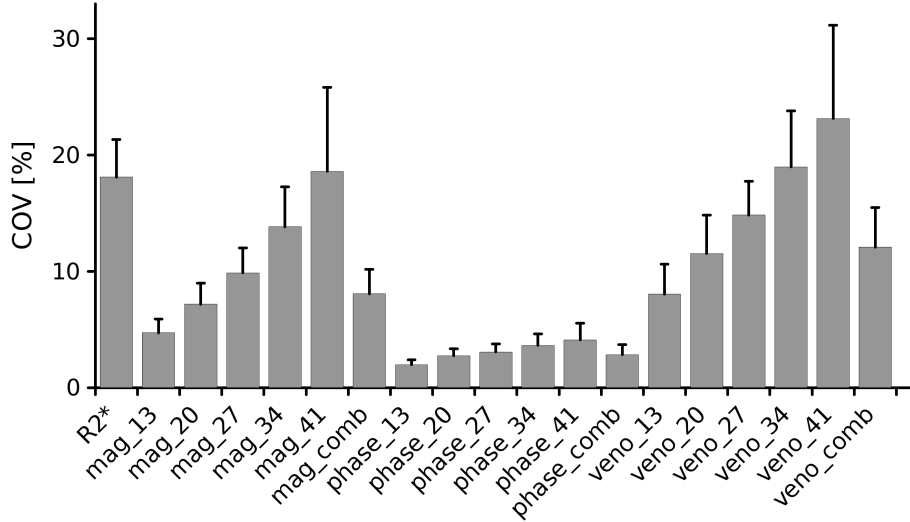


Figure 8.2.: The mean \pm SD COV of all 19 metrics of the left lateral part of the substantia nigra pars compacta (the indices indicate the individual echo times or the combined five echoes). The COV is significantly (only the p-value of the least significant ROI is shown $p = 0.001$) lower in phase images compared to all other metrics. Due to lower signal at later echo times SNR decreases, which results in a higher average COV. The higher SNR in the combined metrics results in lower COV values compared to echo times of 27 ms and longer.

The COV of the combined data showed lower COV than the individual later echoes (three to five) and comparable COV values to the first two echoes. This trend was observed in all other ROIs. Therefore, only the results for R_2^* and the combined data for all ROI are shown in Fig. 8.3. The ROIs are sorted according to their average ROI-volume ascending from left to right in all figures. Phase showed the lowest COV (only the p-value of the least significant ROI is shown) and therefore highest reproducibility in all ROIs compared to R_2^* ($p = 0.0002$), magnitude ($p = 0.0014$) and venogram ($p = 0.0013$). R_2^* showed significantly highest COV compared to the magnitude ($p = 0.0002$) and venogram ($p = 0.005$). Reproducibility was significantly higher in the magnitude than in the venograms ($p = 0.01$).

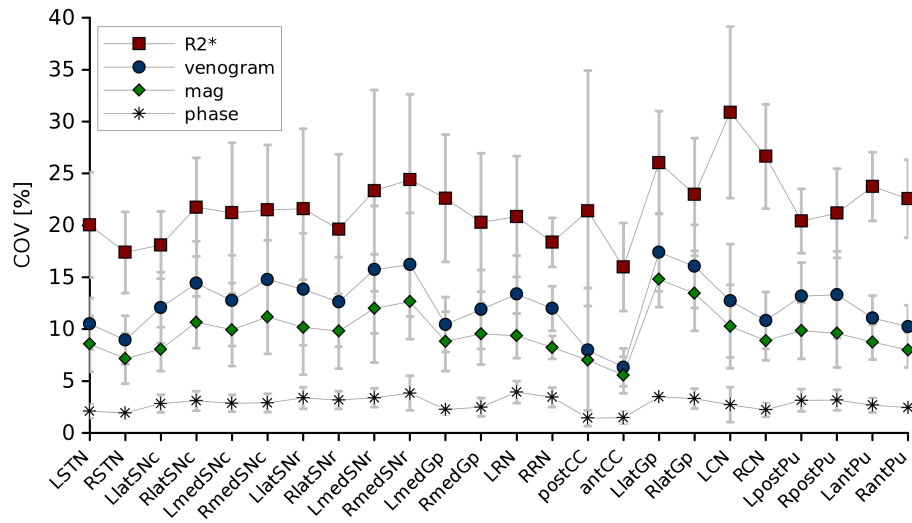


Figure 8.3.: Mean \pm SD COV of the combined echo data of phase, magnitude, venogram and R_2^* . In all ROIs phase had the significantly lowest ($p = 0.001$) and R_2^* the highest ($p = 0.01$) COV. All metrics showed a similar trend throughout the ROIs, as indicated by the lines between the ROIs.

Mean \pm SD of the individual echoes and combined of phase (Fig. 8.4) and R_2^* values (Fig. 8.5) were computed for all regions by averaging over all subjects.

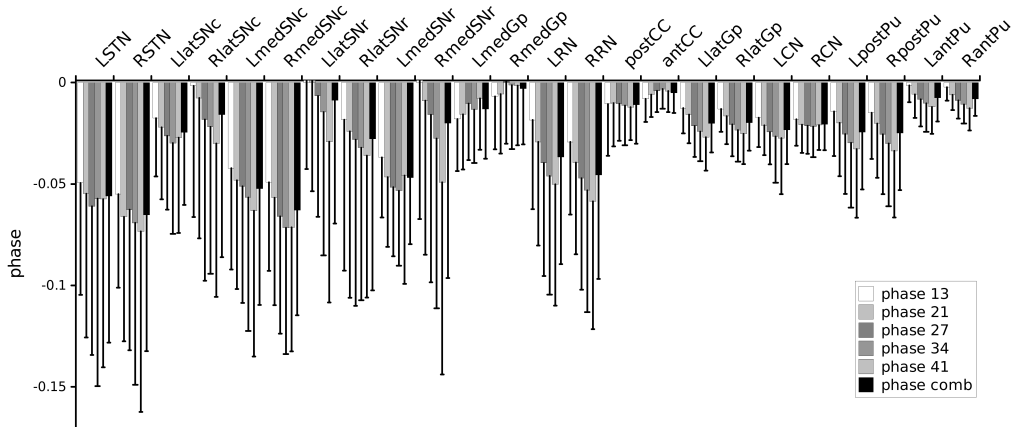


Figure 8.4.: Phase values (mean \pm SD) of the five echoes and the combined data. Phase decreases linearly with TE. No significant difference between the ROI on the left and right hemisphere was found.

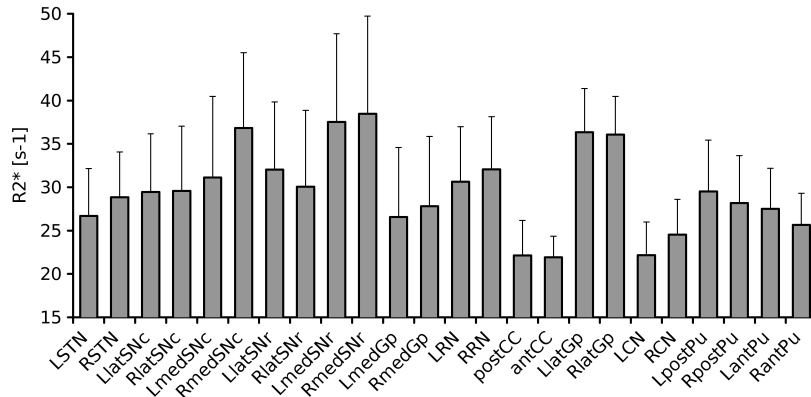


Figure 8.5.: R_2^* values over all subjects in all ROIs. There is a significant difference in R_2^* between the left and right medSNc ($p = 0.04$), LCN ($p = 0.015$) and the antPu ($p = 0.05$).

No significant phase difference was found between ROIs in the left and right hemisphere. A significant difference in R_2^* was only found between the left and right medSNc ($p = 0.04$), LCN ($p = 0.015$) and antPu ($p = 0.05$). The thalamostriate vein showed a significantly higher COV ($p = 0.002$), R_2^* ($p = 0.02$) values and significantly lower phase value ($p = 0.002$) compared to the subependymal vein. No significant differences between the hemispheres were found in R_2^* , phase and COV (Fig. 8.6).

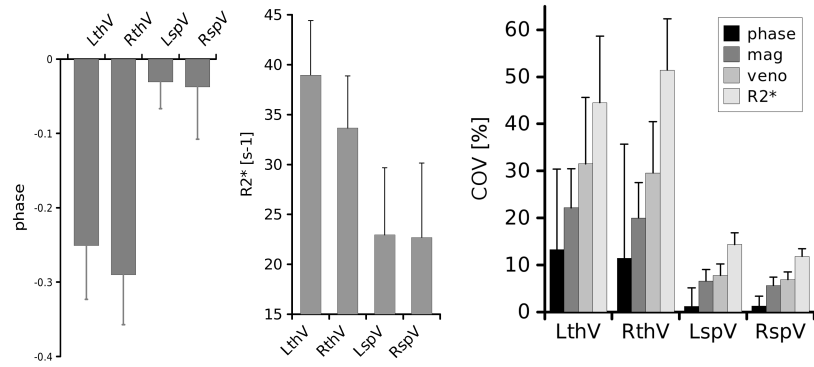


Figure 8.6.: Comparison of R_2^* , phase and COV values between left and right thalamostriate and subependymal vein. There was no significant difference ($p = 0.06$) between the left and right hemisphere in R_2^* , phase and COV. There were significant differences between the thV and spV in phase ($p = 0.002$), R_2^* ($p = 0.02$) and COV ($p = 0.002$). The COV is larger in larger veins and in both types of veins the phase has the lowest COV, followed by magnitude, venogram and R_2^* .

The changes in the COV due to complex and spatial smoothing of R_2^* are displayed in Fig. 8.7. All smoothing filters lead to reduced COV in the ROI. The strongest reductions in COV were obtained with Gaussian smoothing, where the COV decreased on average by 26% with an $3 \times 3 \times 2$ kernel, by about 37% with the $5 \times 5 \times 3$ kernel and by about 46% with the $7 \times 7 \times 5$ kernel. The decrease with the median filter was 9% with the $3 \times 3 \times 2$, 20% with the $5 \times 5 \times 3$ and 31% with the $7 \times 7 \times 5$ kernel.

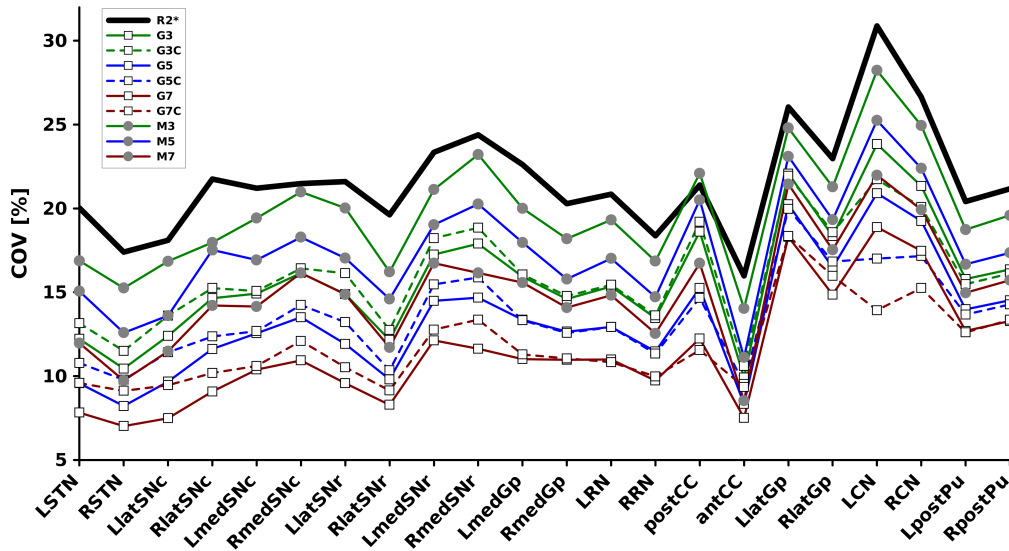


Figure 8.7.: The influence of complex and spatial smoothing on the COV in the ROIs. Both smoothing approaches resulted in a lower COV and therefore a higher reproducibility. Lowest COV values were achieved with Gaussian smoothing. There were no significant differences in COV between smoothing of the magnitude and smoothing of the complex data.

The effect of smoothing of the magnitude images and different spatial resolution at data acquisition on R_2^* is presented in Fig. 8.8 and Figure 8.9. The simulation of larger voxel sizes by complex smoothing increased intravoxel dephasing and therefore also increased R_2^* . The frontal areas of the brain and areas above the nasal sinus show the largest increases in R_2^* with increasing voxel size (Fig. 8.8 G3C, G5C and G7C).

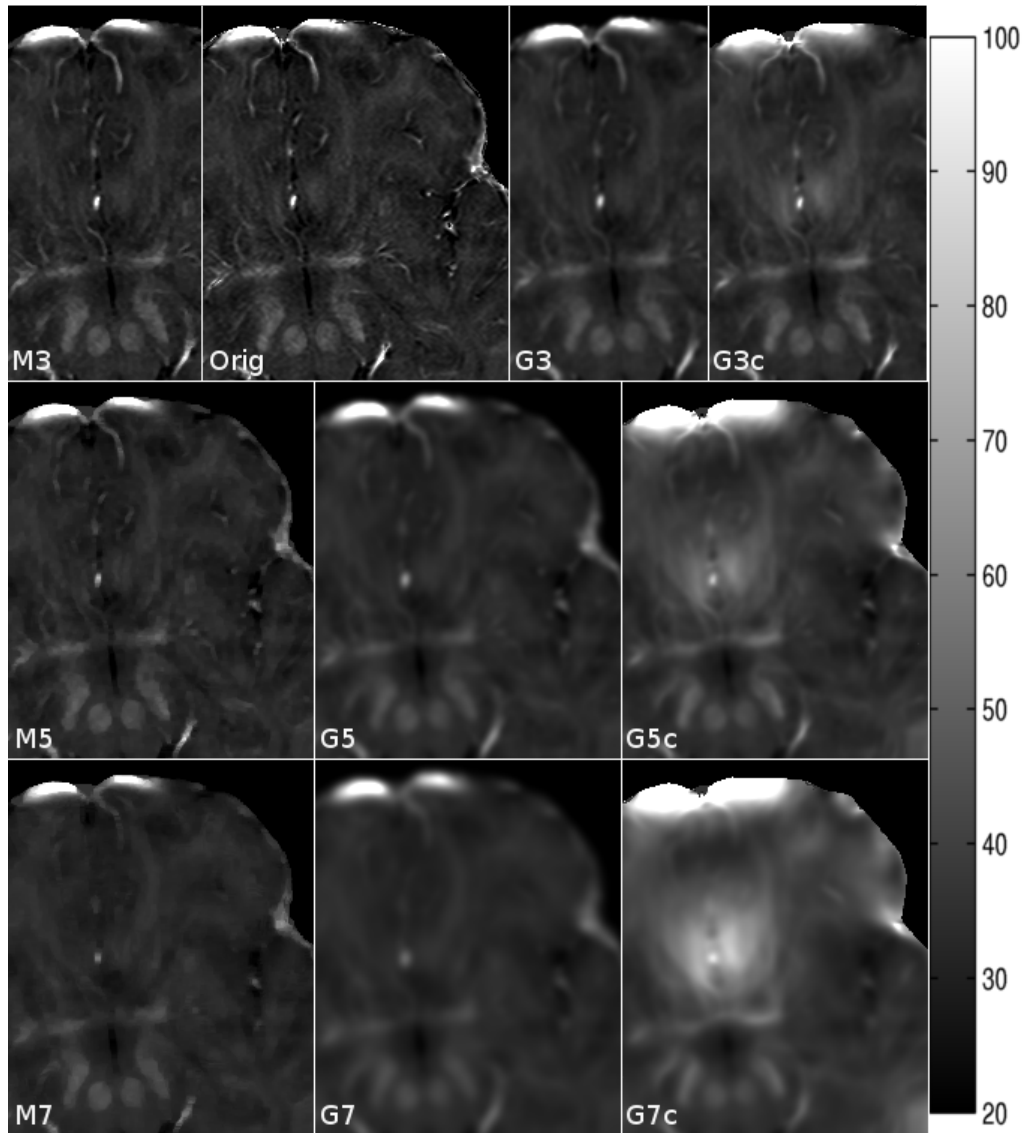


Figure 8.8.: Representative slice of the calculated R_2^* map (Orig) of deep brain regions and the visual changes due to complex and spatial smoothing. With increasing filter kernel size the image structures get blurrier. Gaussian filtering smooths edges of structures; however, median filtering tends to preserve these structures and edges better. The simulation of higher voxel dimensions (complex smoothing labeled with c) led to higher intravoxel dephasing in areas with higher background field inhomogeneities, hence stronger signal loss in the magnitude and highlighted R_2^* areas.

Complex smoothing accelerated R_2^* relaxation within all ROIs (Fig. 8.9). With the $3 \times 3 \times 2$ kernel R_2^* increased on average over all ROI by 4.7%, the $5 \times 5 \times 3$ 9% and the $7 \times 7 \times 5$ voxel filter with 17.3%.

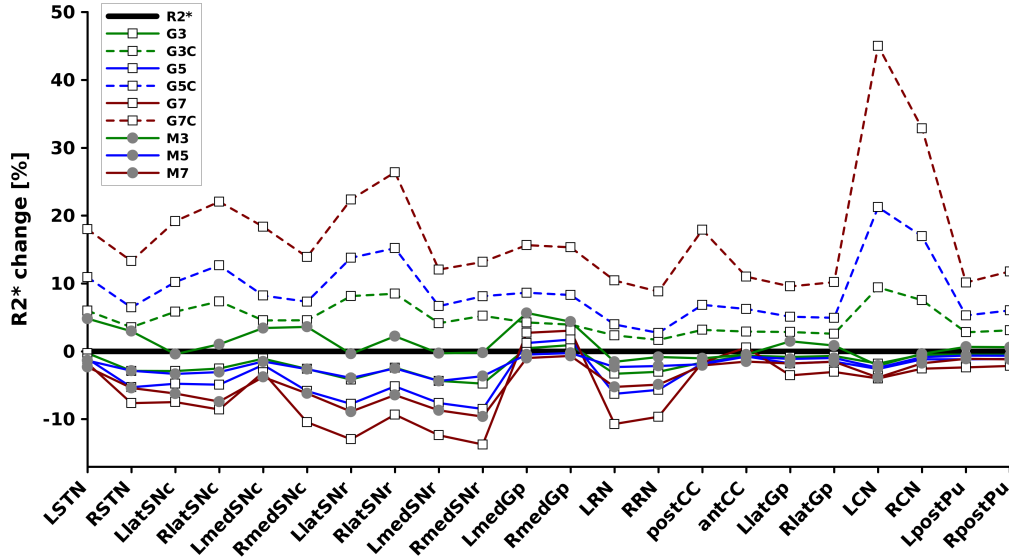


Figure 8.9.: Changes of R_2^* values due smoothing of the magnitude and the complex data. The ROI are sorted by their average ROI-volume ascending from left to right. Complex smoothing resulted in an increase in R_2^* proportional to the kernel size. This increase was independent of the average ROI volume. In ROIs larger than 16 mm^3 (CC) magnitude smoothing did not produce significant changes in R_2^* .

Smoothing of the magnitude images resulted in a general decrease of R_2^* . Significant decreases in R_2^* were observed only with an averaged ROI volume smaller than 16 mm^3 . Larger ROI structures showed no significant changes from the original R_2^* . Gaussian filtering with a $3 \times 3 \times 2$, $5 \times 5 \times 3$ and $7 \times 7 \times 5$ voxel kernel decreased R_2^* on average between 2.3 to 6.9% only within structures smaller than 16 mm^3 . Median filtering with a $3 \times 3 \times 2$ voxel kernel lead to a slight increase in R_2^* by 1.6%. Filter sizes of $5 \times 5 \times 3$ and $7 \times 7 \times 5$ voxels produced a decrease by 2.4 and 5.3% in R_2^* , respectively.

9

Discussion

9.1. SWI with multiple echoes

Susceptibility weighted imaging with a multi echo approach offers a variety of advantages over the single echo technique. Conventional SWI uses a low readout bandwidth to improve SNR. This is necessary because of the small voxel sizes and it is possible because of the long echo times. The increased bandwidth required for the relatively short inter-echo delay of 7 ms in this multi echo method results in a reduction of geometric distortions, smaller chemical shifts and reduced blurring along the readout direction. The resulting SNR penalty per echo is more than compensated by the acquisition of several echoes and therefore longer signal acquisition time. The total data acquisition length (number of echoes divided by the readout bandwidth in Hertz per pixel) of the multi echo sequence is 32 ms compared to 9 ms for single echo data. Furthermore, maps of R_2^* relaxation can be computed.

One caveat is that only the first echo is fully flow compensated. The second and the fourth echo are not flow compensated and the third and fifth echo are only flow compensated along the readout direction [53]. Large arterial vessels may therefore experience signal loss due to fast flow and could be mistaken for veins in the later echoes.

SWI benefits from the reconstruction of multi channel data using the SENSE algorithm [54] which results in unfiltered (but not unwrapped) phase images. Both unwrapping and homodyne filtering can be performed on these images. Homodyne filtering is a robust technique for the generation of high pass filtered phase images. In contrast to standard SWI processing with a fixed filter width for different echo times the homodyne filter width to account for the increased spatial density of phase wraps at later echo times was adjusted. Deistung et al. [42] investigated the influence of different parameters of the homodyne filter at 1.5 T and an echo time of 40 to 50 ms. They reported that a 2D filter window in k-space with a size of 20 to 25 % of the respective k-space dimension leads to good phase contrast and suppression of phase wraps. Since the phase associated with field inhomogeneities scales linearly with $B_0 \times TE$, a filter size of 0.25 at the TE of 20 ms and adjusted the size according to the other echo times was used. This resulted in the expected reduction of phase wraps in the images acquired at later echo times.

The correction of R_2^* for background field inhomogeneities requires unfiltered phase images where all spatial frequencies are preserved. If the phase does not wrap during the time between two echoes, the field map can be computed directly by the complex division of two subsequent echoes. In this study an inter-echo delay of 7 ms was used to allow for high spatial resolution and to cover a broad range of echo times. Long inter-echo delays result in good SNR of the field maps [69] but also in phase wraps in areas with strong background inhomogeneities which have to be removed by phase unwrapping.

The R_2^* values determined with this high resolution 5-echo method are in good agreement with the values reported in the literature [55] [52] [56]. It should be mentioned that the concept of R_2^* fails near venous vessels because R_2^* is only defined for an exponential decay. Since the frequency distribution around a venous vessel is non-Lorentzian, the decay is non-exponential and even a partial signal recovery can occur at late echo times [19]. This fact and that vessel orientation and partial volume effects have a strong influence on the signal formation around a vein [19] explain the large standard deviation of the ' R_2^* ' of venous vessels observed in this study. For the computation of R_2^* maps, full flow compensation is not relevant because R_2^* is not defined in these regions, since the decay due to field inhomogeneities associated with veins is not exponential [19]. That this technique provides venograms perfectly coregistered with the R_2^* maps allows the exclusion of larger veins from region of interest based analysis.

The strong increase in SNR and CNR compared to the single echo magnitude images should be interpreted carefully because SNR measurements are difficult to perform in images obtained with phased array coils [54]. It is impossible to obtain a reliable noise measurement by placing a region of interest into the background of images acquired with phased array coils. Therefore the standard deviation of a region placed in white matter, assuming that the signal variation due to tissue heterogeneity is constant over the different echo times was computed. No absolute SNR values can be determined with this approach but since the same regions were used in the magnitude images in the single echo data and in the multi echo data a qualitative comparison is feasible. Moreover, only minor variations in the standard deviation for the same noise region at the five echo times were found.

Despite these limitations, an increase in SNR and CNR was found in all regions of interest. Although no definite quantitative values can be given, the SNR and CNR increase in all evaluated regions is in good agreement with the overall visual impression of the images. The increase in SNR found in this study is also in agreement with a study by Brainovich et al. [70] who found an increase in SNR by 48 % in dual echo SWI compared to the single echo method using a bird cage head coil at 3 T and a readout bandwidth of 79 Hz/pixel for both echoes. Recently Helms and Dechent [71] presented a thorough investigation of the effects of multi echo averaging. One of their conclusions was that sampling beyond 25 ms is not recommended because background inhomogeneities cause considerable signal drop out in the orbitofrontal cortex. This is true for the voxel sizes employed in typical GRE ($1 - 2\text{mm}^3$). SWI, on the other hand, acquires data with a voxel size of 0.5mm^3 or smaller. The influence of background gradients is therefore reduced compared to lower spatial resolutions [71] allowing for longer echo times.

In conclusion this technique allows the computation of phase images with high contrast, high quality venograms, field maps and high resolution R_2^* maps. The proposed technique comes at almost no cost in terms of data acquisition time and it allows for a joint analysis of R_2^* and phase at high spatial resolution.

9.2. Reproducibility of phase and R_2^*

The reproducibility of phase, magnitude, venograms and R_2^* maps calculated from multi echo SWI data was investigated. The phase's higher SNR compared to the magnitude [37], explains its low COV, i.e. its high reproducibility. The comparatively low reproducibility of R_2^* can be explained by the higher standard deviation of the magnitude at later echo times which affects the fitting procedure. The combination of phase, magnitude and venograms of the the individual echoes leads to an increased SNR and CNR [51] compared to a single echo scan with the same acquisition time, which is also reflected in the improved reproducibility of the combined data. Peran et al. found an average COV over 18 subjects of 24% Pèran et al. [55]. This value was computed for the whole brain on a voxel by voxel basis and therefore includes areas with strong background inhomogeneities. On the other hand, the data were acquired with a voxel volume of $1.5 \times 1.5 \times 2 \text{ mm}^3$ and Gaussian smoothing with a kernel of 3 mm full width at half maximum was applied to the images. This is in agreement with this study where it is found that large voxels and smoothing lead to a reduction in COV.

Smoothing of the magnitude data or data acquisition with lower spatial resolution results in improved SNR and better reproducibility of the R_2^* map. It should be emphasized, however, that there is a difference between acquiring data at low spatial resolution and the smoothing of high spatial resolution data. At low spatial resolution intravoxel spin dephasing due to background field inhomogeneities leads to accelerated R_2^* relaxation compared to high spatial resolutions [66]. To demonstrate this effect smoothing on the complex data was performed, which mimics data acquisition at lower spatial resolution. Magnitude data has also been smoothed. As expected, the R_2^* maps computed after complex smoothing exhibited areas of increased R_2^* , which coincide with regions with strong background field inhomogeneities. Gaussian smoothing of the magnitude data, on the other hand, led to a reduction in R_2^* . This reduction is less pronounced in larger ROIs compared to small ROIs. The reduction is explained by choice of ROIs which were placed mainly in iron rich deep brain structures so that adjacent regions have lower R_2^* than the ROIs. The blurring across boundaries between regions of large R_2^* and low R_2^* has less influence in large ROIs. Therefore, the blurring across tissue boundaries due to smoothing has a stronger effect on smaller ROIs than larger ones.

The R_2^* values determined with the high resolution 5-echo method are in

agreement with the values reported in the literature [51] [52] [72] [55] [73]. Figure 9.1 shows a comparison of five R_2^* studies for representative brain structures. The relaxation rates are consistent with the findings of this study if differences in voxel size and post processing are taken into account. In previous studies the highest relaxation rates were found with large voxel-sizes and when no correction for background inhomogeneities was employed [52] [72] [55]. Peran et al. [55] used smaller voxels than Du et al. [52] and also no background correction, but they applied Gaussian smoothing to the data. In this study, this leads to a reduction of R_2^* by up to 15%. Yao et al. [72] used $1 \times 1 \times 2 \text{ mm}^3$ voxels and no background correction, which is in agreement with their intermediate R_2^* values. Finally, Peters et al. [73] used large voxels of $2.1 \times 2.1 \times 3 \text{ mm}^3$, but they also corrected for decay due to background inhomogeneities. In the caudate nuclei they found values which are in good agreement with all studies, except Du et al. [52]. In the putamen, on the other hand, they report larger R_2^* values compared to the other four studies.

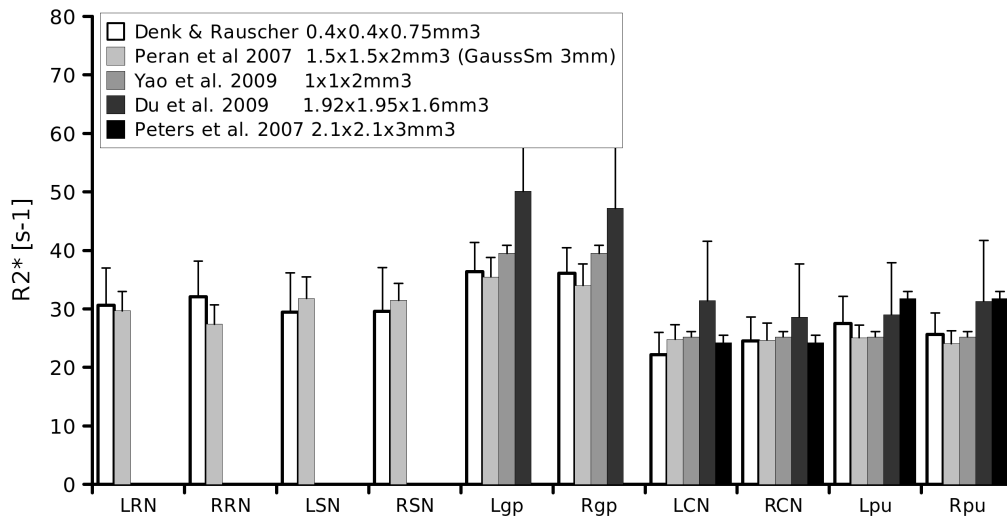


Figure 9.1.: Comparison of extracted R_2^* values from this study with R_2^* values from literature [52] [72] [55] [73].

We did not find significant inter-hemispheric differences in the phase in any of the ROIs. This is in contrast to a study conducted by [62]. However, Xu et al. [62] investigated 78 subjects compared to 12 subjects in this study.

Another somewhat counter-intuitive finding is the smaller COV of phase at shorter echo time. However, if one assumes a complex number with a cer-

tain amount of noise in the real and imaginary part, the noise in the phase is smaller for larger magnitudes than for smaller magnitudes. Therefore, COV decreases with increasing echo time, i.e. with decreasing signal magnitude. This study has some limitations. The registration introduces some degree of smoothing due to the interpolation. However, this smoothing is negligible compared to the quasi-smoothing by averaging over whole regions of interest. The statistics could be improved by scanning the subjects more than twice, which, however would not change the overall findings of this work. Since both phase and R_2^* of white matter depend on the integrity of white matter structure and on the angle between white matter fibres and the main magnetic field, the analysis was limited to deep grey matter regions and veins. Deep grey matter is isotropic and the orientation of the tissue itself does not have an influence on the measured parameters.

The COV is significantly higher in larger veins (thalamostriate) than in smaller (subependymal) veins, which may be explained by partial volume effects and by potential changes in blood oxygenation between the two scans. Caffeine intake 30 minutes to an hour before an MRI scan, for instance, can reduce the signal in veins by up to 25% [74]. Neither were the subjects instructed to follow a certain diet nor did the intake caffeine has been monitored. Apart from blood oxygenation, also the geometrical relationship between veins and voxels plays a role. Even if vessels are not visible in the data due to low spatial resolution, their influence may still be present in R_2^* maps or maps of neural activation. Veins oriented other than parallel to the main magnetic field produce extravascular field inhomogeneities. Therefore, changes in the position of a vein with respect to a voxel changes the signal in that voxel [19] [20]. This means that even if the head orientation is exactly the same in both scans, the position of the veins inside the voxels still has an influence on the signal.

In conclusion, it is shown that phase has a higher reproducibility than magnitude data or R_2^* maps. The R_2^* maps and their reproducibility depend on the acquisition matrix and post processing. Lower spatial resolution (as simulated by complex smoothing) may increase SNR but it also changes R_2^* values because of an increased sensitivity to background field inhomogeneities. These findings suggest that acquisition at high spatial resolution for reduced sensitivity to background field inhomogeneities followed by smoothing of the magnitude data gives the most robust results.

Acronyms

ant anterior
BOLD blood oxygen level depend
BW band width
CC corpus callosum
CN caudate nucleus
CNR contrast to noise ratio
COV coefficient of variation
CSF cerebro spinal fluid
FA flip angle
FID free induction decay
fMRI functional magnetic resonance imaging
FOV field of view
FSL FMRIB Software Library
FW filter width
Gp globus pallidus
GRE gradient echo
GM grey matter
lat lateral
med medial
mIP minimal intensity projections
MRI magnetic resonance imaging
NMR nuclear magnetic resonance
pos posterior
Pu putamen
RF radio frequency
RN red nucleus
ROI region of interest
SAR specific absorption rate
SD standard deviation
SE spin echo

SENSE sensitivity encoding
SN substantia nigra
SNc substantia nigra pars compacta
SNr substantia nigra pars reticulata
SNR signal to noise ratio
STN subthalamic nucleus
SWI susceptibility weighted imaging
TE echo time
TR repetition time
VV voxel volume
WM white matter

Danksagung

An dieser Stelle möchte ich mich besonders bei Alexander Rauscher ("the man who would be rather skiing") für seine dauerhafte Unterstützung, die spannenden Diskussionen und für den ein oder anderen 'kurzen' Schispaziergang bedanken. Weiters möchte ich mich herzlich bei Prof. Rattay für die Betreuung meiner Masterarbeit bedanken. Besonderer Dank gilt Prof. Wolfgang Grisold der mir vor 4 Jahren die Welt der Wissenschaft näher gebracht hat.

Furthermore i like to thank especially everyone from the UBC MRI Research Centre for all their help, discussions and time: Alex MacKay, Nino, Davis, Coree, Irene, Kelly, Saed, Sandra.

Dank gebührt ebenfalls allen Mitarbeitern der Arbeitsgruppe am Hochfeld MR Zentrum am AKH Wien: Prof. Trattinig, Wolfgang, Stephan und Günther.

Muchas gracias tambien a la gente en la Facultad de Ingeniería Biomédica en Valparaiso: Steren, Alejandro, Angelo, Camila, Ruben.

Ganz besonderer Dank gilt meinen Eltern die mich über all die Jahre in allen Zielen unterstützt haben. Meiner Schwester kann ich gar nicht genug danken, da Sie bei Tag oder Nacht immer mit Rat und Tat zur Seite stand und weiterhin steht. Und schließlich an all jene die meine Tage verschönern oder verschönert haben: Anna, Babsi, Claudi, Christoph, Eva, Joe, Petrina, Roberto, Werner, ...

Bibliography

- [1] J. R. Reichenbach and E. M. Haacke, “High-resolution BOLD venographic imaging: a window into brain function,” *NMR in Biomedicine*, vol. 14, pp. 453–67, Nov. 2001.
- [2] E. M. Haacke, Y. Xu, Y. N. Cheng, and J. R. Reichenbach, “Susceptibility weighted imaging (SWI),” *Magnetic Resonance in Medicine*, vol. 52, pp. 612–8, Sept. 2004.
- [3] S. Mittal, Z. Wu, J. Neelavalli, and E. M. Haacke, “Susceptibility-weighted imaging: technical aspects and clinical applications, part 2,” *AJNR. American Journal of Neuroradiology*, vol. 30, pp. 232–252, Feb. 2009.
- [4] K. A. Tong, S. Ashwal, B. A. Holshouser, J. P. Nickerson, C. J. Wall, L. A. Shutter, R. J. Osterdock, E. M. Haacke, and D. Kido, “Diffuse axonal injury in children: clinical correlation with hemorrhagic lesions,” *Annals of Neurology*, vol. 56, pp. 36–50, July 2004.
- [5] J. Park, S. Park, S. Kang, T. Nam, B. Min, and S. Hwang, “Detection of traumatic cerebral microbleeds by susceptibility-weighted image of MRI,” *Journal of Korean Neurosurgical Society*, vol. 46, pp. 365–369, Oct. 2009.
- [6] N. D. Wycliffe, J. Choe, B. Holshouser, U. E. Oyoyo, E. M. Haacke, and D. K. Kido, “Reliability in detection of hemorrhage in acute stroke by a new three-dimensional gradient recalled echo susceptibility-weighted

- imaging technique compared to computed tomography: a retrospective study,” *Journal of Magnetic Resonance Imaging: JMRI*, vol. 20, pp. 372–377, Sept. 2004.
- [7] K. Santhosh, C. Kesavadas, B. Thomas, A. K. Gupta, K. Thamburaj, and T. R. Kapilamoorthy, “Susceptibility weighted imaging: a new tool in magnetic resonance imaging of stroke,” *Clinical Radiology*, vol. 64, no. 1, pp. 74–83, 2009.
- [8] M. Ayaz, A. S. Boikov, E. M. Haacke, D. K. Kido, and W. M. Kirsch, “Imaging cerebral microbleeds using susceptibility weighted imaging: one step toward detecting vascular dementia,” *Journal of Magnetic Resonance Imaging: JMRI*, vol. 31, no. 1, pp. 142–148, 2010.
- [9] Y. Tsui, F. Y. Tsai, A. N. Hasso, F. Greensite, and B. V. Nguyen, “Susceptibility-weighted imaging for differential diagnosis of cerebral vascular pathology: a pictorial review,” *Journal of the Neurological Sciences*, vol. 287, pp. 7–16, Dec. 2009.
- [10] W. Zhang, X. Ma, Y. Ji, X. Kang, and C. Li, “Haemorrhage detection in brain metastases of lung cancer patients using magnetic resonance imaging,” *The Journal of International Medical Research*, vol. 37, pp. 1139–1144, Aug. 2009.
- [11] C. Li, B. Ai, Y. Li, H. Qi, and L. Wu, “Susceptibility-weighted imaging in grading brain astrocytomas,” *European Journal of Radiology*, Aug. 2009.
- [12] D. Berg, H. Hochstrasser, K. J. Schweitzer, and O. Riess, “Disturbance of iron metabolism in parkinson’s disease – ultrasonography as a biomarker,” *Neurotoxicity Research*, vol. 9, no. 1, pp. 1–13, 2006.
- [13] P. D. Griffiths, B. R. Dobson, G. R. Jones, and D. T. Clarke, “Iron in the basal ganglia in parkinson’s disease. an in vitro study using extended x-ray absorption fine structure and cryo-electron microscopy,” *Brain: A Journal of Neurology*, vol. 122 (Pt 4), pp. 667–673, Apr. 1999.

- [14] S. M. Levine and A. Chakrabarty, “The role of iron in the pathogenesis of experimental allergic encephalomyelitis and multiple sclerosis,” *Annals of the New York Academy of Sciences*, vol. 1012, pp. 252–266, Mar. 2004.
- [15] P. Zamboni, “The big idea: iron-dependent inflammation in venous disease and proposed parallels in multiple sclerosis,” *Journal of the Royal Society of Medicine*, vol. 99, pp. 589–593, Nov. 2006.
- [16] G. Bartzokis, J. Cummings, S. Perlman, D. B. Hance, and J. Mintz, “Increased basal ganglia iron levels in huntington disease,” *Archives of Neurology*, vol. 56, pp. 569–574, May 1999.
- [17] C. M. Morris, J. M. Kerwin, and J. A. Edwardson, “Non-haem iron histochemistry of the normal and alzheimer’s disease hippocampus,” *Neurodegeneration*, vol. 3, pp. 267–275, Dec. 1994.
- [18] A. Fatemi-Ardekani, C. Boylan, and M. D. Noseworthy, “Identification of breast calcification using magnetic resonance imaging,” *Medical Physics*, vol. 36, pp. 5429–5436, Dec. 2009. PMID: 20095255.
- [19] J. Sedlacik, A. Rauscher, and J. R. Reichenbach, “Obtaining blood oxygenation levels from MR signal behavior in the presence of single venous vessels,” *Magnetic Resonance in Medicine*, vol. 58, pp. 1035–1044, Nov. 2007.
- [20] A. Deistung, A. Rauscher, J. Sedlacik, J. Stadler, S. Witoszynskij, and J. R. Reichenbach, “Susceptibility weighted imaging at ultra high magnetic field strengths: theoretical considerations and experimental results,” *Magnetic Resonance Imaging*, vol. 60, pp. 1155–1168, Nov. 2008.
- [21] A. Rauscher, J. Sedlacik, M. Barth, E. M. Haacke, and J. R. Reichenbach, “Noninvasive assessment of vascular architecture and function during modulated blood oxygenation using susceptibility weighted

- magnetic resonance imaging,” *Magnetic Resonance in Medicine*, vol. 54, pp. 87–95, July 2005.
- [22] G. Hoiting, *Measuring MRI noise*. PhD thesis, University of Groningen, Groningen, 2005.
- [23] E. M. Haacke, R. W. Brown, M. R. Thompson, and R. Venkatesan, *Magnetic Resonance Imaging: Physical Principles and Sequence Design*. Wiley-Liss, 1st ed., June 1999.
- [24] R. A. D. Graaf, *In vivo NMR spectroscopy: principles and techniques*. Wiley Chichester, 1998.
- [25] A. Rauscher, *Phase Information in Magnetic Resonance Imaging*. PhD thesis, Vienna University of Technology, Vienna, 2005.
- [26] S. Ljunggren, “A simple graphical representation of fourier-based imaging methods,” *J. Magn. Reson*, vol. 54, no. 2, pp. 338–343, 1983.
- [27] D. B. Twieg, “The k-trajectory formulation of the NMR imaging process with applications in analysis and synthesis of imaging methods,” *Medical Physics*, vol. 10, no. 5, pp. 610–621, 1983.
- [28] W. A. Edelstein, J. M. Hutchison, G. Johnson, and T. Redpath, “Spin warp NMR imaging and applications to human whole-body imaging,” *Physics in Medicine and Biology*, vol. 25, pp. 751–756, July 1980.
- [29] D. A. Yablonskiy and E. M. Haacke, “Theory of NMR signal behavior in magnetically inhomogeneous tissues: the static dephasing regime,” *Magnetic Resonance in Medicine*, vol. 32, pp. 749–763, Dec. 1994.
- [30] L. Pauling and C. D. Coryell, “The magnetic properties and structure of hemoglobin, oxyhemoglobin and carbonmonoxyhemoglobin,” *Proceedings of the National Academy of Sciences of the United States of America*, vol. 22, pp. 210–216, Apr. 1936.

- [31] R. M. Weisskoff and S. Kiihne, "MRI susceptometry: image-based measurement of absolute susceptibility of MR contrast agents and human blood," *Magnetic Resonance in Medicine*, vol. 24, pp. 375–383, Apr. 1992.
- [32] S. Ogawa, T. M. Lee, A. R. Kay, and D. W. Tank, "Brain magnetic resonance imaging with contrast dependent on blood oxygenation," *Proceedings of the National Academy of Sciences of the United States of America*, vol. 87, pp. 9868–9872, Dec. 1990.
- [33] S. Ogawa, T. M. Lee, A. S. Nayak, and P. Glynn, "Oxygenation-sensitive contrast in magnetic resonance image of rodent brain at high magnetic fields," *Magnetic Resonance in Medicine*, vol. 14, pp. 68–78, Apr. 1990.
- [34] C. Springer, *NMR in Physiology and Biomedicine*. Academic Press, 1994.
- [35] B. Hallgren and P. Sourander, "The effect of age on the non-haemin iron in the human brain," *Journal of Neurochemistry*, vol. 3, pp. 41–51, Oct. 1958. 13611557.
- [36] A. Rauscher, J. Sedlacik, M. Barth, H. Mentzel, and J. R. Reichenbach, "Magnetic susceptibility-weighted MR phase imaging of the human brain," *AJNR. American Journal of Neuroradiology*, vol. 26, pp. 736–42, Apr. 2005.
- [37] J. H. Duyn, P. van Gelderen, T. Li, J. A. de Zwart, A. P. Koretsky, and M. Fukunaga, "High-field MRI of brain cortical substructure based on signal phase," *Proceedings of the National Academy of Sciences of the United States of America*, vol. 104, pp. 11796–801, July 2007.
- [38] D. C. Noll, D. G. Nishimura, and A. Macovski, "Homodyne detection in magnetic resonance imaging," *IEEE Transactions on Medical Imaging*, vol. 10, no. 2, pp. 154–63, 1991.

- [39] S. Witoszynskyj, A. Rauscher, J. R. Reichenbach, and M. Barth, "Phase unwrapping of MR images using PhiUN - a fast and robust region growing algorithm," *Medical Image Analysis*, Oct. 2008.
- [40] S. Chavez, Q. Xiang, and L. An, "Understanding phase maps in MRI: a new cutline phase unwrapping method," *IEEE Transactions on Medical Imaging*, vol. 21, pp. 966–977, Aug. 2002.
- [41] W. Xu and I. Cumming, "A region-growing algorithm for InSAR phase unwrapping," *IEEE transactions on geoscience and remote sensing*, vol. 37, no. 1, pp. 124–134, 1999.
- [42] A. Deistung, A. Rauscher, J. Sedlacik, S. Witoszynskyj, and J. Reichenbach, "Optimization of data processing in Susceptibility-Weighted imaging," *International Conference of Medical Physics*, vol. 14, p. 1168, 2005.
- [43] E. M. Haacke, S. Mittal, Z. Wu, J. Neelavalli, and Y. N. Cheng, "Susceptibility-weighted imaging: technical aspects and clinical applications, part 1," *AJNR. American Journal of Neuroradiology*, vol. 30, no. 1, pp. 19–30, 2009.
- [44] J. F. Schenck and E. A. Zimmerman, "High-field magnetic resonance imaging of brain iron: birth of a biomarker?," *NMR in Biomedicine*, vol. 17, pp. 433–445, Nov. 2004.
- [45] M. A. Fernández-Seara and F. W. Wehrli, "Postprocessing technique to correct for background gradients in image-based R_2^* measurements," *Magnetic Resonance in Medicine*, vol. 44, pp. 358–66, Sept. 2000.
- [46] H. Dahnke and T. Schaeffter, "Limits of detection of SPIO at 3.0 T using T_2 relaxometry," *Magnetic Resonance in Medicine*, vol. 53, pp. 1202–6, May 2005.
- [47] W. R. W. Martin, M. Wieler, and M. Gee, "Midbrain iron content

- in early parkinson disease: a potential biomarker of disease status,” *Neurology*, vol. 70, pp. 1411–7, Apr. 2008.
- [48] Y. P. Du, R. Chu, D. Hwang, M. S. Brown, B. K. Kleinschmidt-DeMasters, D. Singel, and J. H. Simon, “Fast multislice mapping of the myelin water fraction using multicompartment analysis of T_2^* decay at 3T: a preliminary postmortem study,” *Magnetic Resonance in Medicine*, vol. 58, pp. 865–870, Nov. 2007.
- [49] R. Ogg, J. W. Langston, E. M. Haacke, R. G. Steen, and J. S. Taylor, “The correlation between phase shifts in gradient-echo MR images and regional brain iron concentration,” *Magnetic Resonance Imaging*, vol. 17, pp. 1141–1148, Oct. 1999.
- [50] J. R. Reichenbach, R. Venkatesan, D. J. Schillinger, D. K. Kido, and E. M. Haacke, “Small vessels in the human brain: MR venography with deoxyhemoglobin as an intrinsic contrast agent,” *Radiology*, vol. 204, pp. 272–7, July 1997.
- [51] C. Denk and A. Rauscher, “Susceptibility weighted imaging with multiple echoes,” *Journal of Magnetic Resonance Imaging: JMRI*, vol. 31, no. 1, pp. 185–191, 2010.
- [52] Y. P. Du, Z. Jin, Y. Hu, and J. Tanabe, “Multi-echo acquisition of MR angiography and venography of the brain at 3 tesla,” *Journal of Magnetic Resonance Imaging: JMRI*, vol. 30, pp. 449–454, Aug. 2009.
- [53] A. Deistung, E. Dittrich, J. Sedlacik, A. Rauscher, and J. R. Reichenbach, “ToF-SWI: simultaneous time of flight and fully flow compensated susceptibility weighted imaging,” *Journal of Magnetic Resonance Imaging: JMRI*, vol. 29, pp. 1478–1484, June 2009.
- [54] K. P. Pruessmann, M. Weiger, M. B. Scheidegger, and P. Boesiger, “SENSE: sensitivity encoding for fast MRI,” *Magnetic Resonance in Medicine*, vol. 42, pp. 952–62, Nov. 1999.

- [55] P. Péran, G. Hagberg, G. Luccichenti, A. Cherubini, V. Brainovich, P. Celsis, C. Caltagirone, and U. Sabatini, “Voxel-based analysis of R_2^* maps in the healthy human brain,” *Journal of Magnetic Resonance Imaging: JMRI*, vol. 26, pp. 1413–1420, Dec. 2007.
- [56] G. Krüger and G. H. Glover, “Physiological noise in oxygenation-sensitive magnetic resonance imaging,” *Magnetic Resonance in Medicine*, vol. 46, pp. 631–637, Oct. 2001.
- [57] J. F. Schenck, “MR safety at high magnetic fields,” *Magnetic Resonance Imaging Clinics of North America*, vol. 6, pp. 715–730, Nov. 1998.
- [58] S. A. Gronemeyer, J. W. Langston, S. L. Hanna, and J. W. Langston, “MR imaging detection of calcified intracranial lesions and differentiation from iron-laden lesions,” *Journal of Magnetic Resonance Imaging: JMRI*, vol. 2, pp. 271–276, June 1992.
- [59] E. M. Haacke, N. Y. C. Cheng, M. J. House, Q. Liu, J. Neelavalli, R. J. Ogg, A. Khan, M. Ayaz, W. Kirsch, and A. Obenaus, “Imaging iron stores in the brain using magnetic resonance imaging,” *Magnetic Resonance Imaging*, vol. 23, no. 1, pp. 1–25, 2005.
- [60] C. M. Morris and J. A. Edwardson, “Iron histochemistry of the substantia nigra in parkinson’s disease,” *Neurodegeneration*, vol. 3, pp. 277–282, Dec. 1994.
- [61] E. M. Haacke, M. Ayaz, A. Khan, E. S. Manova, B. Krishnamurthy, L. Gollapalli, C. Ciulla, I. Kim, F. Petersen, and W. Kirsch, “Establishing a baseline phase behavior in magnetic resonance imaging to determine normal vs. abnormal iron content in the brain,” *Journal of Magnetic Resonance Imaging: JMRI*, vol. 26, pp. 256–264, Aug. 2007.
- [62] X. Xu, Q. Wang, and M. Zhang, “Age, gender, and hemispheric differences in iron deposition in the human brain: an in vivo MRI study,” *NeuroImage*, vol. 40, pp. 35–42, Mar. 2008.

- [63] R. J. Ordidge, J. M. Gorell, J. C. Deniau, R. A. Knight, and J. A. Helpert, "Assessment of relative brain iron concentrations using T_2 -weighted and T_2^* -weighted MRI at 3 tesla," *Magnetic Resonance in Medicine*, vol. 32, pp. 335–341, Sept. 1994.
- [64] J. M. Gorell, R. J. Ordidge, G. G. Brown, J. C. Deniau, N. M. Buderer, and J. A. Helpert, "Increased iron-related MRI contrast in the substantia nigra in parkinson's disease," *Neurology*, vol. 45, pp. 1138–1143, June 1995.
- [65] S. C. Chu, Y. Xu, J. A. Balschi, and C. S. Springer, "Bulk magnetic susceptibility shifts in NMR studies of compartmentalized samples: use of paramagnetic reagents," *Magnetic Resonance in Medicine*, vol. 13, pp. 239–262, Feb. 1990.
- [66] J. R. Reichenbach, R. Venkatesan, D. A. Yablonskiy, M. R. Thompson, S. Lai, and E. M. Haacke, "Theory and application of static field inhomogeneity effects in gradient-echo imaging," *Journal of Magnetic Resonance Imaging: JMRI*, vol. 7, pp. 266–279, Apr. 1997.
- [67] A. Rauscher, M. Barth, J. R. Reichenbach, R. Stollberger, and E. Moser, "Automated unwrapping of MR phase images applied to BOLD MR-venography at 3 tesla," *Journal of Magnetic Resonance Imaging: JMRI*, vol. 18, pp. 175–80, Aug. 2003.
- [68] S. M. Smith, M. Jenkinson, M. W. Woolrich, C. F. Beckmann, T. E. J. Behrens, H. Johansen-Berg, P. R. Bannister, M. D. Luca, I. Drobnjak, D. E. Flitney, R. K. Niazy, J. Saunders, J. Vickers, Y. Zhang, N. D. Stefano, J. M. Brady, and P. M. Matthews, "Advances in functional and structural MR image analysis and implementation as FSL," *NeuroImage*, vol. 23 Suppl 1, pp. S208–219, 2004.
- [69] C. Hutton, A. Bork, O. Josephs, R. Deichmann, J. Ashburner, and R. Turner, "Image distortion correction in fMRI: a quantitative evaluation," *NeuroImage*, vol. 16, pp. 217–240, May 2002.

- [70] V. Brainovich, U. Sabatini, and G. E. Hagberg, “Advantages of using multiple-echo image combination and asymmetric triangular phase masking in magnetic resonance venography at 3T,” *Magnetic Resonance Imaging*, vol. 27, no. 1, pp. 23–37, 2009.
- [71] G. Helms and P. Dechent, “Increased SNR and reduced distortions by averaging multiple gradient echo signals in 3D FLASH imaging of the human brain at 3T,” *Journal of Magnetic Resonance Imaging: JMRI*, vol. 29, no. 1, pp. 198–204, 2009.
- [72] B. Yao, T. Li, P. van Gelderen, K. Shmueli, J. A. de Zwart, and J. H. Duyn, “Susceptibility contrast in high field MRI of human brain as a function of tissue iron content,” *NeuroImage*, vol. 44, pp. 1259–1266, Feb. 2009.
- [73] A. M. Peters, M. J. Brookes, F. G. Hoogenraad, P. A. Gowland, S. T. Francis, P. G. Morris, and R. Bowtell, “ T_2^* measurements in human brain at 1.5, 3 and 7T,” *Magnetic Resonance Imaging*, vol. 25, pp. 748–753, jul 2007.
- [74] J. Sedlacik, K. Helm, A. Rauscher, J. Stadler, H. Mentzel, and J. R. Reichenbach, “Investigations on the effect of caffeine on cerebral venous vessel contrast by using susceptibility-weighted imaging (SWI) at 1.5, 3 and 7T,” *NeuroImage*, vol. 40, pp. 11–18, Mar. 2008.